

# **The Role of the Plasmasphere in Radiation Belt Particle Energization and Loss**

by

Wm. Robert Johnston

A research proposal submitted to the faculty of  
the University of Texas at Dallas  
in partial fulfillment of the requirements  
for the degree of Doctor of Philosophy

12 September 2007

## Abstract

The plasmapause separates cold dense plasma in the inner magnetosphere from hot, low-density outer magnetosphere plasma. This boundary is very dynamic in response to changes in magnetospheric convection and other stormtime phenomena. The outer radiation belt is also dynamic during stormtime in terms of both radial location and energetic particle population. It is proposed that outer radiation belt particles are variously depleted and energized due to wave-particle interactions inside and outside the plasmasphere. Testing this hypothesis requires simultaneous observations of energetic particles and the plasmapause location. We derive plasmapause locations using DMSP identifications of the plasmapause signature in the ionosphere, specifically the light ion trough (LIT). This offers significantly improved temporal coverage given the continuous multiyear coverage by multiple DMSP satellites and the overlapping radiation belt observations by SAMPEX. The LIT location is semi-automatically identified from DMSP RPA observations of light ion densities, then mapped along magnetic field lines to the plasmapause. Initial comparisons show good agreement between these plasmapause locations and those obtained from IMAGE EUV observations. Case studies also show good correlations between DMSP-identified plasmapause locations and SAMPEX observations of outer radiation belt particle distributions and precipitating particle microbursts. This approach will eventually provide an extensive database of plasmapause locations, permitting us to quantify the relationship between the LIT and the plasmapause, and improve understanding of the relationship between the plasmapause location and the outer radiation belt.

# Contents

<b>1</b>	<b>Introduction</b>	<b>3</b>
<b>2</b>	<b>Background</b>	<b>5</b>
2.1	Plasmasphere . . . . .	5
2.2	Ionosphere . . . . .	15
2.3	Radiation belts . . . . .	19
<b>3</b>	<b>Instruments</b>	<b>27</b>
3.1	DMSP . . . . .	27
3.2	IMAGE . . . . .	31
3.3	SAMPEX . . . . .	32
3.4	ACE . . . . .	35
<b>4</b>	<b>Method and Initial Results</b>	<b>38</b>
4.1	LIT identification . . . . .	39
4.2	Mapping to plasmasphere . . . . .	43
4.3	Comparison to IMAGE observations . . . . .	47
4.4	Comparison to SAMPEX observations . . . . .	52

<b>5</b>	<b>Continuing Research</b>	<b>58</b>
5.1	Planned work . . . . .	58
5.2	Timetable . . . . .	61
<b>6</b>	<b>Summary and Conclusion</b>	<b>63</b>
<b>7</b>	<b>List of Acronyms</b>	<b>64</b>
<b>8</b>	<b>References</b>	<b>67</b>

# Chapter 1

## Introduction

The Earth's radiation belts are recognized as very dynamic, with this behavior tied to dynamics of the plasmasphere. Many efforts are underway to observe, model, and explain the dynamics of the trapped particle populations and their interactions with plasma waves and other magnetospheric phenomena. One limitation in these efforts is the lack of extensive observations of the plasmopause with continuity in time. We propose to develop a multi-year database of plasmopause identifications based on DMSP observations, then to statistically study the correlations between these locations and the dynamics of trapped particle populations. This study is highly relevant and timely to ongoing space physics community efforts.

We first review the plasmasphere, including its structure both in steady state and in active time conditions; ionospheric signatures of the plasmopause; and the radiation belts, particularly the connection between the outer electron belt and the plasmasphere via wave-particle interactions. We then describe the spacecraft instruments from which we will use data: instruments on DMSP, IMAGE, SAMPEX, and ACE. We then discuss

the data analysis procedure, results thus far, and the plan of work. The procedure and results include progress in development of the semi-automated method for extracting the plasmopause from DMSP light ion density data; mapping these identifications to the high-altitude plasmopause, including comparisons with IMAGE observations; and comparisons with SAMPEX observations of energetic electrons. Future plans include development of the plasmopause database and statistical comparison of this database to SAMPEX observations.

# Chapter 2

## Background

### 2.1 Plasmasphere

**Magnetosphere.** The magnetosphere (Figure 2.1) results from the interaction of the Earth's magnetic field and plasma environment with the solar wind and interplanetary magnetic field (IMF). The terrestrial magnetic field is approximately a dipolar field with its axis inclined  $11^\circ$  to the Earth's rotation axis. Interaction with the solar wind and IMF compresses the geomagnetic field on the sunward side and produces an extended antisunward magnetotail; the magnetopause separates the enclosed geomagnetic cavity from the IMF. Solar wind plasma encounters the magnetopause, with differing gyromotions depending on particle charge, resulting in the magnetopause current around the sides of the magnetosphere. This magnetopause boundary region is also called the magnetosheath. The magnetopause distance from the Earth in the direction of the Sun is of order  $10R_E$ , but this is variable with solar wind and IMF conditions.

The motion of the solar wind past the geomagnetic cavity produces a cross tail electric

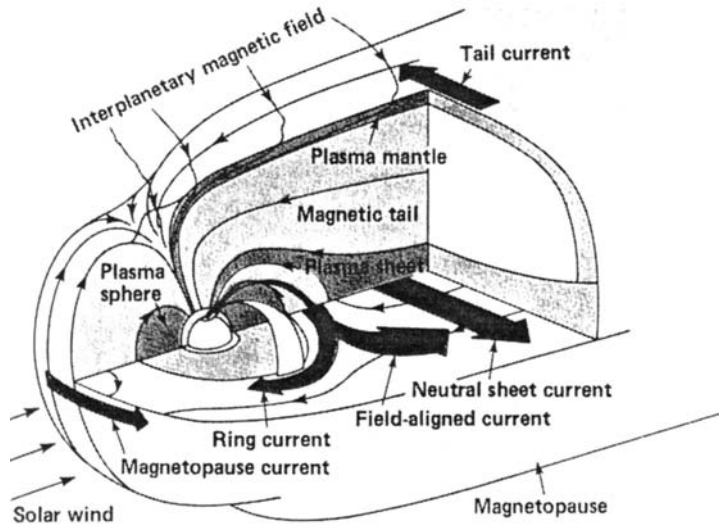


Figure 2.1: Magnetosphere structure and current systems (from Hargreaves, 1992).

field and a sunward convection of plasma up the tail. The cross tail electric field is essentially the  $\mathbf{v} \times \mathbf{B}$  field resulting from solar wind velocity  $\mathbf{v}$  past the magnetic field  $\mathbf{B}$  at the magnetopause. Sunward convection is understood to result both from viscous interaction between magnetosphere plasma and the solar wind at the magnetopause and from the effects of linkage between the IMF and geomagnetic fields. The resulting sunward moving plasmasheet is thin in the vertical direction, corresponding to the sharp gradient between sunward and antisunward magnetic field lines dragged from the geomagnetic field. Plasma particles undergo both gradient drift and curvature as they approach the Earth, causing drift of ions westward and electrons eastward around the Earth. The result is the ring current, directed westward around the Earth. Ring current intensity is highly dependent on geomagnetic activity and is indirectly measurable by ground-based magnetometers, contributing to the Dst index. Another phenomena where the plasmasheet approaches the Earth is formation of polarization electric fields which tend to “shield”



the inner magnetosphere from the external electric fields. These shielding electric fields respond to changing solar wind/IMF conditions on a timescale of minutes. Because of this delay, overshielding or undershielding can result during active periods; such imbalances are called penetration electric fields.

Near the geomagnetic poles, geomagnetic field lines connect to the magnetopause and thence to the IMF. At the Earth this region of open field lines is called the polar cap; it is surrounded by the auroral oval, where field lines are stretched through the tail plasmasheet or through the magnetosheath. Energetic particles from these sources are guided along magnetic field lines until they collide with particles in the Earth's atmosphere, resulting in the aurorae themselves.

**Plasmasphere, introduction.** The plasmasphere is a torus of plasma in the innermost region of the magnetosphere, comprising the corotating region of the magnetosphere. Magnetic field lines there are closed and approximately dipolar, permitting filling of the plasmasphere by plasma escaping from the Earth's ionosphere. Plasmasphere plasma is mostly  $H^+$  at high densities ( $10$  to  $10^3 \text{ cm}^{-3}$ ) and low temperatures ( $\sim 1 \text{ eV}$ ) relative to the rest of the magnetosphere, with the plasmapause being the boundary between these regions. The plasmasphere was independently identified by in situ plasma measurements and ground-based whistler observations in the early 1960s. Gringauz (1963) used plasma observations from the Lunik Moon probes to identify a steep density gradient corresponding to the outer edge of the plasmasphere. Carpenter (1963) used observations of whistlers, radio waves propagating along geomagnetic field lines, to identify this same density gradient (Figure 2.2a). Later in the 1960s the basic theoretical picture of the steady state plasmasphere emerged. Observations from a variety of satellites have since helped identify it as quite dynamic. In 2000 the IMAGE satellite began providing direct imagery of the

plasmasphere from outside (Figure 2.2b), showing a range of plasmaspheric structure.

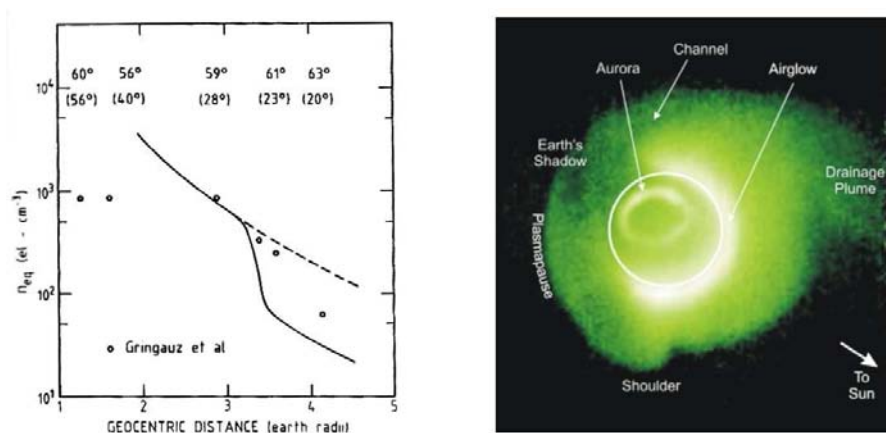


Figure 2.2: Illustrative plasmasphere observations. a) Early plasmasphere density observations. Solid line shows density vs. location as derived from whistler observations, as opposed to the expected gradient (dashed line). Points indicate Lunik density measurements (figure from Lemaire and Gringauz, 1998). b) Illustrative IMAGE EUV (30.4 nm) observation of plasmasphere, taken 24 May 2000 from  $6.0 R_E$  and MLAT= $73^\circ$  (from Sandel et al., 2003).

**Steady state models.** To first order, the plasmasphere is the region in the inner magnetosphere where the corotation electric field dominates over the cross tail electric field. The cross tail electric field, directed from dawn to dusk, tends to produce equipotentials parallel to the Sun-Earth axis. The geomagnetic field, rotating with the Earth, produces a  $\mathbf{v} \times \mathbf{B}$  electric field about the Earth. The outer boundary of the plasmasphere, the plasmapause, is approximately where these two fields are equal, i.e. near an  $L$  value such that

$$E_T = \frac{B_E}{L^3} L R_E \omega \quad (2.1)$$

where  $E_T$  is the cross tail field,  $B_E$  is the magnetic field strength at the Earth's surface and equator ( $B_E = 0.31$  G),  $R_E$  is the Earth's radius, and  $\omega$  is the Earth's rotational speed. The  $L$  value is a convenient parameter for a fixed field line and is the radial distance from the field axis to the field line intersection with the magnetic equator (i.e. its greatest radial distance) expressed in terms of the Earth's radius  $R_E$ . For a typical plasmapause location of  $L=4$ ,  $E_T = 1$  mV/m. Plasma convection in the magnetosphere, generally sunward, is channeled along equipotentials in this combined electric field, while plasma within the plasmapause corotates with the Earth. This basic model, shown in Figure 2.3, was proposed soon after discovery of the plasmasphere (Nishida, 1966; Brice, 1967).

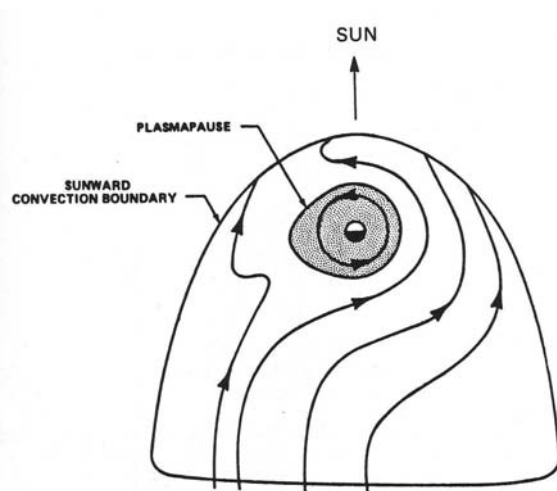


Figure 2.3: Magnetospheric plasma convection in the tail and plasmasphere (from Hargreaves, 1992).

Magnetic field lines in the plasmasphere are closed and nearly dipolar. The toroidal surface of the plasmasphere intersects the Earth's surface at high latitudes (for  $L = 4$ ,

MLAT=60°), roughly corresponding to the equatorward boundary of the auroral zone. Beyond the plasmasphere, magnetic field lines are drawn antisunward and stretched down the magnetotail on the nightside. The closed magnetic flux tubes within the plasmasphere fill with escaping ionospheric plasma on a timescale of days.

An early modification to the simple convection-corotation model is the Stern-Volland model (Volland, 1973; Stern, 1975), which includes a semi-empirical shielding effect. These previously mentioned shielding electric fields result from polarization in the plasmasheet as it approaches the Earth, tending to shield the inner magnetosphere from the convection electric field. The convection-corotation model discussed above gives a potential

$$\Phi = -E_T y - B_E \omega \frac{R_E^3}{r}, \quad (2.2)$$

where  $y$  is in GSM coordinates and  $r$  is the radial distance from the center of the Earth; the first term is from convection (constant crosstail electric field) and the second from corotation. In contrast, the Stern-Volland model as typically applied replaces the convection term with a semi-empirical term:

$$\Phi = -A_0 y r - B_E \omega \frac{R_E^3}{r} = A_0 r^\gamma \sin \theta - B_E \omega \frac{R_E^3}{r} \quad (2.3)$$

for  $\gamma = 2$ , with  $\theta$  the angle in MLT relative to noon. Note that the generalized form containing  $\gamma$  reduces to the convection-corotation model for  $\gamma = 1$ . In practice the constant  $A_0$  is often determined empirically, although it can be derived observationally, e.g. from cross-polar cap potentials (Goldstein et al., 2005a). Such models have shown some success at reproducing plasmasphere evolution, particularly when the Stern-Volland field is parameterized with time and thus allowed to vary with  $K_p$ . However, they still fail to reproduce some structures, and other sources of electric fields must be taken into account,

as noted by Goldstein et al. (2003). Models such as the Rice Convection Model treat plasma motion in self-consistently determined electric fields, reproducing shielding as well as other electric fields (Toffoletto et al., 2003).

**Stormtime changes.** Even in the 1960s, study of the plasmasphere showed dynamic behavior in response to solar activity and geomagnetic conditions. The basic convection-corotation model suggests a teardrop shape that will change in size with changes in solar and/or geomagnetic activity. These changes are observed along with additional storm-related dynamics and structure.

During periods of high geomagnetic activity, the region of closed field lines is compressed closer to the Earth. At such times the plasmopause may be at  $L = 2$ , compared to  $L = 4 - 6$  in typical conditions. When considered relative to  $K_p$  index, the response in plasmopause location is delayed on the order of hours. Carpenter and Park (1973) found an empirical relation for the plasmopause location of

$$L_{pp} = 5.7 - 0.47K_p, \quad (2.4)$$

valid for the midnight-dawn sector and using the maximum  $K_p$  index value over the preceding 12 hours. Other published versions of this relation include some incorporating MLT dependence. O'Brien and Moldwin (2003) used CRRES-observed plasmopause crossings from 1990 to 1991 to produce relationships using  $K_p$ , Dst, and AE indices, for various time delays and for both the form above and MLT dependence. As an example, their results using  $K_p$  gave the MLT-independent form

$$L_{pp} = 5.9 - 0.43K_p \quad (2.5)$$

and the MLT-dependent form

$$L_{pp} = -0.39 \left[ 1 - 0.34 \cos \left( \frac{\text{MLT} - 16.6}{24/2\pi} \right) \right] K_p + 5.6 \left[ 1 + 0.12 \cos \left( \frac{\text{MLT} - 3}{24/2\pi} \right) \right], \quad (2.6)$$

both using the maximum  $K_p$  for the preceding 36 hours. Similarly good fits were obtained for AE and Dst index fits; for all three indices, fits were best on the day side and worst on the dusk side.

The delayed response of plasmapause location to these indices is partly explainable in terms of erosion and refilling processes. The quiet time plasmasphere comprises plasma-filled flux tubes on closed corotating convection paths. Onset of a geomagnetic storm strengthens the crosstail convection electric field, opening the convection paths of the outermost flux tubes and allowing them to empty plasma out the dayside magnetopause. This permits depletion of plasma from these flux tubes, although Carpenter and Lemaire (1997) note that a significant fraction of eroded plasma may remain within the outer magnetosphere for some time. Until this erosion is complete, the plasmapause (in terms of density gradient) is outside the corotation limit. When activity drops and convection returns to its previous state, the now empty flux tubes just inside the convection-corotation boundary slowly refill with ionospheric plasma over hours to days. During refilling, the plasmapause (in terms of density gradient) is inward of the corotation limit. Two density knees have been observed during refilling, with a second plasmapause inward of the main (outer) plasmapause (Horwitz et al., 1986), and refilling is not steady over time, with a two-stage process possible (Dent et al., 2006). Such temporal evolution of the plasmasphere has been modeled by Rasmussen et al. (1993); their two-dimensional model includes resupply of  $H^+$  from the ionosphere, effects of convection and corotation, and saturation of flux tubes. They obtain timescales of 3 to 100 days for 90% refilling depending on  $L$  value and time during solar cycle.

**Dayside bulge.** The simple model of plasmapause shape driven by combined corotation and convection electric fields suggests a teardrop shape with a duskside bulge (Figure

2.3). The duskside bulge is indeed observed, but the bulge exhibits more dynamical behavior than this model would imply and is understood to be related to additional phenomena. Chappell et al. (1971a) found structure including regions of dense plasma on the dayside apparently detached from the main plasmasphere (these may relate to drainage plumes since identified by IMAGE observations). Similarly, the bulge was also found to be disconnected. Moldwin et al. (1994) characterized bulge dynamics using observations from several geosynchronous satellites. With circular equatorial orbits at  $6.62R_E$ , such satellites often encounter the plasmapause duskside bulge. The bulge was usually centered in the duskside, but the location varied significantly and varied most significantly for quiet time conditions.

**Plasmasphere structures.** Plasmasphere erosion and refilling during episodes of changing convection were described previously. IMAGE has permitted observation of details of this process along with the discovery of a variety of structural features, including plumes, shoulders, and notches.

Drainage plumes tend to be observed in the noon-to-dusk sector during periods of erosion. Figure 2.4 shows a sequence of observations showing the pre-erosion plasmasphere, a sunward convection surge of plasma following contraction of the corotation region, and the evolution of a sunward plasma plume. The process, to first order, is consistent with the picture of plasmasphere response to changing convection electric field (Li and Xu, 2005). Goldstein and Sandel (2005) interpreted the large-scale behavior in the event shown in Figure 2.4 as the result of dayside magnetopause reconnection during southward IMF; this reconnection drives magnetospheric convection changes with effects on the plasmasphere. However, they note some differences between their model and observations, probably associated with subauroral and penetration electric fields. Plumes such as these

have been observed to wrap around the plasmasphere, as the plume base rotates with the plasmasphere, resulting in channels (Sandel et al., 2003). This may partly explain older observations of “detached” plasmas on the dayside by Chappell et al. (1971a). Plumes may also be observed as multiple plateaus in density profiles, such as those in DE-1 observations reported by Horwitz et al. (1990b).

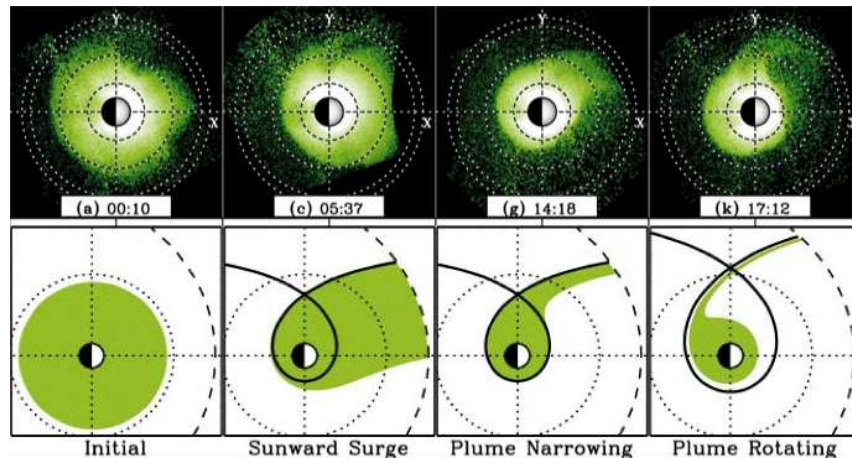


Figure 2.4: Sequence of IMAGE EUV observations (top) on 18 June 2001 showing plasmasphere erosion and plume formation, with idealized representation (bottom) (from Goldstein, 2004).

Notches are deep radial evacuated features in the outer plasmasphere boundary. These features may extend over  $2R_E$  in radial distance and 3 hours in MLT in the magnetic equatorial plane. An example is shown in Figure 2.5. Some notches develop a dense inner plasma plume, producing a W- or M-shaped feature (Gallagher et al., 2005); this is common for larger notches (Sandel et al., 2003). While irregularities in the plasmasphere radius of order  $1R_E$  were known by the early 1970s (Carpenter and Park, 1973), only with IMAGE could they be properly characterized. IMAGE has observed notches with



lifetimes up to 60 hours, sufficient to reveal that they typically sub-corotate with an average rotation rate about 90% of corotation (Sandel et al., 2003; Gallagher et al., 2005). This sub-corotation has been explained by Burch et al. (2004) as a result of corotation lag in the upper ionosphere. They correlated IMAGE observations of notches to DMSP observations of ionospheric drifts, i.e. to sub-corotation in the ionosphere. The lag in the upper ionosphere is, they conclude, a result of the disturbance dynamo. During storm times, the auroral ionosphere is heated by particle precipitation and joule heating. The heating produces equatorward winds which are deflected westward by the Coriolis force, producing a lag behind the Earth’s rotation in these regions.



Figure 2.5: IMAGE EUV observation of a notch (lower right) from 4 July 2000 (from Sandel et al., 2006).

## 2.2 Ionosphere

**Introduction.** The ionosphere is the region of the Earth’s atmosphere partially ionized by solar radiation. This plasma density as a function of altitude tends to peak at a few hundred km altitude. The Chapman production function describes this to first order, giv-

ing a characteristic peak above which density declines exponentially due to fewer neutrals available for photoionization, and below which density declines super-exponentially due to rapidly declining penetration of ionizing photons. The actual structure, shown in Figure 2.6, includes the F-region (peak about 300 km) and E-region (lesser peak about 100 km) and differs from the Chapman profile for several reasons. These reasons include differences in photochemistry at different altitudes (contributing to secondary peaks) and variations with latitude, temporal changes in solar radiation, and vertical transport. Above the F-peak, the density decreases with height slower than predicted by the Chapman function. Electrons and ions have very different scale heights due to their differing masses, but any difference in upward diffusion would produce polarization electric fields. The result is a scale height corresponding to the average for the plasma species, both ions and electrons (Kelley and Heelis, 1989). This ambipolar diffusion characterizes plasma diffusion along magnetic field lines in the upper ionosphere as well as the plasmasphere. Dominant ionospheric ion species range from  $O^+$  and molecular ions at lower altitudes to  $He^+$  and  $H^+$  at higher altitudes (of order 800 km to 1500 km). The ionosphere is a conductive medium linked to and interacting with the magnetosphere. Region 2 field aligned currents (FAC), closed through the auroral zone, and region 1 FAC, closed through the polar cap boundary, link to magnetosphere currents including the ring current and magnetosheath current.

**Light ion trough.** The light ion trough (LIT) is the steep latitudinal gradient in  $H^+/He^+$  density observed near the equatorial edge of the auroral zone (Kelley and Heelis, 1989). In the upper ionosphere (at altitudes of 800-1500 km), the dominant ion species are  $O^+$ ,  $H^+$ , and  $He^+$ . The LIT is observed near but generally equatorward of the low latitude auroral boundary, with  $H^+$  concentrations often 10 to  $10^3$  times lower on the high latitude side of this boundary as on the low latitude side. Poleward of the LIT, the light

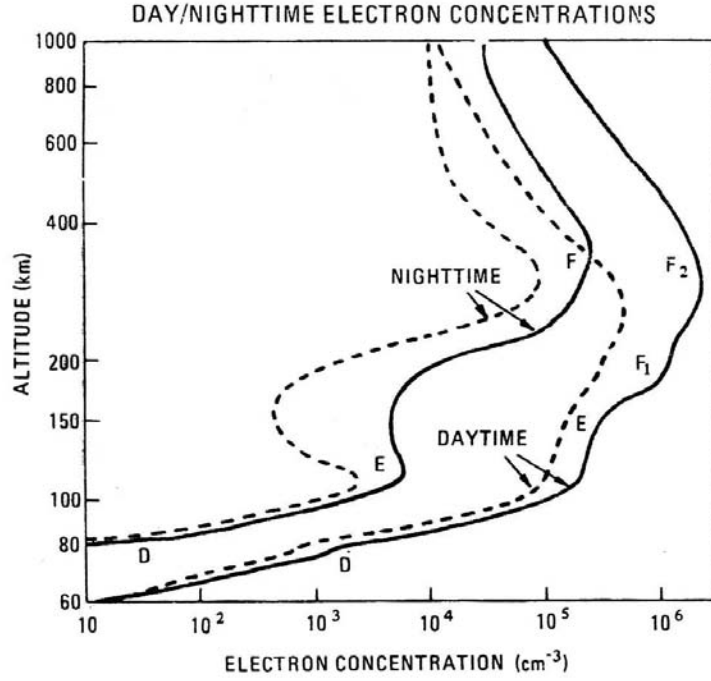


Figure 2.6: Typical ionospheric electron number density profiles (from Tascione, 1988).

ion concentration is depressed by outward field-aligned motions which can be supersonic. The light ion trough is typically not observable below the  $O^+$  transition height, i.e. the height below which  $O^+$  is the dominant species. This height is lower for lower scale heights and consequently for lower temperatures; consequently, day/night conditions and time during solar cycle affect its altitude. Karpachev and Sidorova (2003) studied the LIT in  $He^+$  density using ISS-b data from 1000-1200 km altitude, finding the LIT observable in  $\sim 50\%$  of passes in nighttime winter conditions versus  $\sim 25\%$  in daytime summer conditions.

**Signature of plasmopause.** Many ionospheric signatures of the plasmopause have been proposed. In general, these links are not one-to-one correspondences and suffer

from limitations in simultaneous measurements in both the ionosphere and plasmasphere. Rycroft and Burnell (1970) used Alouette satellite observations to link the midlatitude electron density trough with the plasmapause. This correspondence has also been observed with whistler data (Foster et al., 1978). However, with higher  $K_p$  this trough occurs at lower latitudes than the plasmapause (Kohnlein and Raitt, 1977). Yizengaw et al. (2005) and Yizengaw and Moldwin (2005) found a good correlation between the plasmapause and the midlatitude trough as identified by total electron content using GPS data. The subauroral electron temperature enhancement (SETE), a latitudinally narrow peak in ionospheric topside electron temperature, was found to coincide with the plasmapause by Brace and Theis (1974) in ISIS-1 data and by Horwitz et al. (1986) in DE-1/DE-2 data. The precipitating electron boundary is also a suggested signature (Foster et al., 1978). Stable auroral red arcs, auroral arcs near 400 km altitude with 630 nm oxygen line emissions, have been found to correspond with the plasmapause (e.g. Chappell et al., 1971b).

A good correspondence (although still not one-to-one) is suggested between the light ion trough and the plasmapause (Taylor and Walsh, 1972). LIT-plasmapause correlation is suggested by a simple model where light ions (with greater scale heights and thermal velocities than  $O^+$ ) escaping from the ionosphere are the source of plasmasphere plasma. Consequently, the density structures and gradients of the plasmasphere and ionospheric light ions are correlated along field lines. Linking ionospheric troughs to the plasmapause has been challenging in part due to lack of simultaneous measurements. Taylor and Walsh (1972) suggested the LIT was one of the more consistent ionospheric plasmapause signatures. Foster et al. (1978), however, found the LIT generally a few degrees equatorward of the plasmapause as identified by whistler waves. They also found limitations in the

correspondence including variations of the thermal plasma density gradient invariant latitude with altitude, possibly resulting from coupling dynamics. Grebowsky et al. (1978) suggested that during refilling of the outer plasmapause, supersonic upward  $H^+$  flows result in the LIT being equatorward of the plasmapause density gradient. They also noted a possible duskside mismatch between the high altitude and low altitude plasmapauses. Horwitz et al. (1990a) found that ionospheric density profiles of light ions (and  $He^+$  in particular) were good indicators of plasmaspheric density structure and gradients.

## 2.3 Radiation belts

**Introduction.** The Earth’s radiation belts (Figure 2.7) include both an inner and outer toroidal region of trapped energetic particles (Spjeldvik and Rothwell, 1985). The inner belt, discovered in 1958 (Van Allen et al., 1959), includes energetic electrons and protons (and other ions). It is located at about  $L = 1.5-2$  and is very stable, with particle lifetimes of years. The outer belt is dominated by energetic electrons, is typically located around  $L = 3-7$ , and is very dynamic in response to geomagnetic activity, e.g. storms resulting from solar wind/IMF interactions with the Earth’s magnetosphere (Baker et al., 2004). The inner edge of the outer radiation belt tends to correspond to the outer edge of the plasmasphere, a region in which magnetic flux tubes are filled by low energy plasma. The two belts are separated by the relatively low radiation “slot” region.

The particle trapping results from charged particle motion in the approximately dipolar magnetic field of the Earth. The three main elements of geomagnetically trapped charged particle motion are shown in Figure 2.7. First,  $\mathbf{v} \times \mathbf{B}$  acceleration causes a charged particle to undergo gyromotion about a magnetic field line, with resulting frequency of order

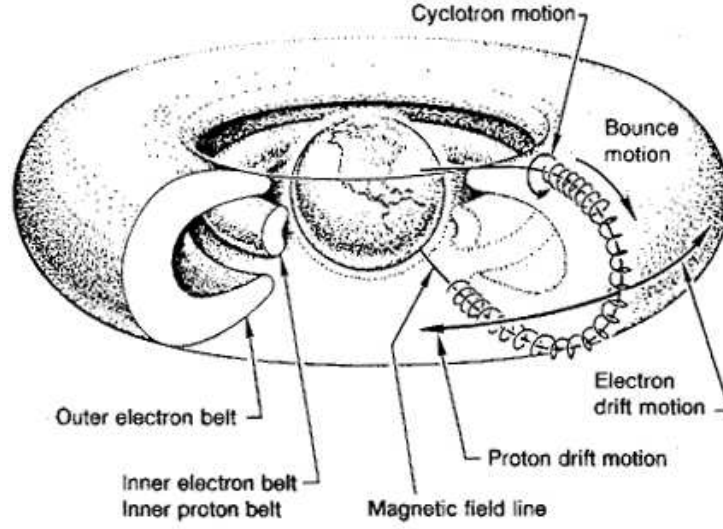


Figure 2.7: Radiation belt structure and periodic motions of trapped particles: gyromotion, bounce motion, and drift motion (from McKay et al., 1992).

kHz. Second, the dipolar field lines curve down toward the Earth into regions of stronger magnetic field, creating a magnetic “bottle”. This produces periodic bounce motion (frequency of order Hz) between lower altitude mirror points. Third, the radial gradient in the magnetic field across the particle’s gyro path induces a drift motion (frequency of order mHz) about the magnetic field axis, with electrons drifting east and protons/ions drifting west.

**Adiabatic invariants.** For each periodic motion, the action integral is approximately constant under appropriate conditions and thus defines an associated adiabatic invariant. The action integral in this context is

$$J_i = \oint_i \left[ \mathbf{p} + \frac{q}{c} \mathbf{A} \right] \cdot d\mathbf{l} \quad (2.7)$$

with particle momentum  $\mathbf{p}$  and magnetic vector potential  $\mathbf{A}$ . The generally used forms of

the invariants for the three motions of magnetically trapped particles are, respectively,

$$\mu = J_1 = \frac{p^2 \sin^2 \alpha}{2m_0 B}, \quad (2.8)$$

$$J = \frac{1}{2}J_2 = \int_{-l_m}^{+l_m} p_{\parallel} dl, \quad (2.9)$$

$$\Phi = \frac{c}{q}J_3 = -\frac{2\pi B_E R_E^2}{L}. \quad (2.10)$$

The first invariant  $\mu$  is the relativistic magnetic moment as a function of particle momentum  $p$ , its pitch angle  $\alpha$  (defined as the angle between the field line and the particle momentum vector), its rest mass  $m_0$ , and the local magnetic field strength  $B$ . The second or longitudinal invariant  $J$  is an integral of  $p_{\parallel}$ , momentum parallel to the field line  $l$ , between the mirror points  $\pm l_m$ . The third invariant  $\Phi$  is magnetic flux; it is expressed in terms of the equatorial magnetic field and radius at the Earth's surface,  $B_E$  and  $R_E$ , respectively, and the  $L$  value.

Conservation of the first adiabatic invariant implies that, in the non-relativistic case, the quantity

$$\frac{\sin^2 \alpha}{B} = \frac{\sin^2 \alpha_0}{B_0} \quad (2.11)$$

is constant. Thus, the particle may be described by the equatorial pitch angle  $\alpha_0$  (with  $B_0$  the equatorial magnetic field strength for the field line the particle is on). During bounce motion the pitch angle then varies from  $\alpha_0$  at the magnetic equator to  $\pi/2$  at the mirror point.

The charged particle population may then be described as functions of  $\mu$ ,  $J$ , and  $\Phi$ , since these are invariants over the periodic motion. For comparison to physical observations, however, a more useful set of parameters is one more directly related to observed parameters, e.g. particle kinetic energy  $\epsilon$ , equatorial pitch angle  $\alpha_0$ , and  $L$  value. The third

invariant  $\Phi$  is uniquely related to  $L$ , i.e.  $\Phi = \Phi(L)$ , but  $\mu = \mu(\epsilon, \alpha_0, L)$  and  $J = J(\epsilon, \alpha_0, L)$ . (Dependence of  $\mu$  on  $L$  results from dependence on local magnetic field strength.) The consequence for modeling dynamics of the radiation belt population is that simulation is best accomplished in a phase space of the invariants (or, equivalently, of  $\mu$ ,  $J$ , and  $L$ ), but then these results are best converted to the space of parameters  $\epsilon$ ,  $\alpha_0$ , and  $L$  for physical interpretation.

It should be noted that at several points (e.g. the above definition of  $\Phi$ ) we assume the magnetic field to be dipolar. This is only approximately true for the Earth, but sufficiently so for our purposes. The magnetic field strength at a given radial distance  $R$  (in terms of  $R_E$ ) and magnetic latitude  $\lambda$  is then

$$B(R, \lambda) = \frac{B_E}{R^3} \sqrt{1 + 3 \sin^2 \lambda}, \quad (2.12)$$

with  $B_E = 0.31$  G (Hargreaves, 1992). At the magnetic equator,  $B = B_0 = B_E/L^3$ .

**Particle sources, diffusion, and losses.** Even ignoring the dynamical behavior of the radiation belts (the outer belt in particular), the quasi-steady state of the radiation belt represents a balance between particle sources, diffusion, and losses. This balance remains a topic of research nearly 50 years after discovery of the radiation belts (also see Schulz and Lanzerotti, 1974).

The evolution of the particle population  $f(\mu, J, \Phi; t)$  may be approximated by

$$\frac{\partial f}{\partial t} = \sum S_i - \sum \frac{f}{\tau_j} + \frac{\partial}{\partial \mu} \left( D_{\mu\mu} \frac{\partial f}{\partial \mu} \right) + \frac{\partial}{\partial J} \left( D_{JJ} \frac{\partial f}{\partial J} \right) + \frac{\partial}{\partial \Phi} \left( D_{\Phi\Phi} \frac{\partial f}{\partial \Phi} \right) \quad (2.13)$$

where  $S_i$ 's represent particle sources,  $\tau_j$ 's represent timescales for particle losses, and the  $D_{xx}$ 's are the diffusion terms. Since diffusion with respect to each invariant tends to be independent, the above equation neglects the diffusion cross-terms. Full three-dimensional



phase space simulations including cross terms have been accomplished, e.g. Beutier and Boscher (1995).

Sources of trapped particles include the solar wind (with particles entering through the outer magnetosphere) and the plasmasheet. Such particles may be energized by wave-particle interactions or crosstail electric field fluctuations. The inward transport and energization of solar wind particles appears to be an important source for the outer belt and is sufficient in models to reproduce an inner belt as well (Lyons and Thorne, 1973; Walt, 1996). Cosmic ray albedo neutron decay, or decay of neutrons produced by cosmic ray collisions in the atmosphere, is also a significant source. In addition to these and other natural sources, high altitude nuclear explosions (such as several tests in 1958-1962) can be significant artificial sources.

Of the many diffusion mechanisms known or proposed, a number involve various wave-particle interactions. In general, particles may be energized or suffer changes in pitch angle due to resonances between an electromagnetic wave and the particle's gyromotion. This includes effects of whistlers, electromagnetic waves (from VLF to ULF) in plasma which travel along magnetic field lines and have velocities dependent on signal frequency and electron density along the propagation path. Other relevant plasma waves include EMIC waves, or electromagnetic ion cyclotron waves. Diffusion in  $\Phi$  (or, equivalently, in  $L$ ) can result from fluctuations in the geomagnetic field. Stormtime variations in the crosstail electric field produce inward diffusion of trapped particles in which diffusion  $\mu$  is approximately conserved, and consequently  $\epsilon$  increases.

Radiation belt particles may be lost through pitch angle scattering when their pitch angle becomes sufficiently small that the mirror point is low enough in the atmosphere to allow collisions with atmospheric particles. The limiting pitch angle  $\alpha_L$  for such loss,

which defines the loss cone, is given by

$$\sin^2 \alpha_L = \frac{1}{\sqrt{4\frac{L^6}{R^6} - 3\frac{L^5}{R^5}}} \quad (2.14)$$

where  $R$  is the radial location of loss to collisions in terms of the Earth's radius  $R_E$ . Scattering into the loss cone (i.e. to values of  $\alpha < \alpha_L$ ) can result from wave-particle interactions, including those from whistler waves described above, or from near collisions with charged particles. Such Coulomb collisions can occur not just in the ionosphere (300-800 km altitude) but throughout the plasmasphere (up to  $L = 3-5$ ). Note that the value of  $R$  for loss in the atmosphere or ionosphere is longitude dependent, since the Earth's magnetic field is offset from the Earth's center (Dessler and O'Brien, 1965). Another loss mechanism is magnetopause shadowing, where particles are lost from drift orbits which carry them outside the magnetopause.

**Wave-particle interactions and the plasmasphere.** As noted above, wave-particle interactions affect the radiation belts by causing energization, diffusion, and loss of particles. The relevant plasma waves (e.g. whistler waves) have different characteristics and different interactions inside and outside the plasmasphere, due to the differing plasma densities and temperatures. EMIC waves are associated with the plasmapause, although not necessarily preferentially there (Fraser and Nguyen, 2001).

Consequently, the evolution of the plasmapause during active times can significantly affect the outer radiation belt. Particle fluxes in the outer belt are generally depleted early in a storm and gradually repopulated over several days during recovery (Baker et al., 1986; Li et al., 1997). During the geomagnetic storm of October 2003, contraction of the plasmapause to  $L = 1.5$  was correlated with displacement of the outer radiation belt inward into the slot region (Baker et al., 2004). Goldstein et al. (2005b), compared the

plasmopause, as identified by IMAGE EUV observations, with SAMPEX radiation belt observations and found that the outer radiation belt responded to radial movement of the plasmopause during disturbed times with a time lag of several days.

Summers et al. (1998) offered a model for plasmasphere-related stormtime dynamics of the outer radiation belt due to wave-particle interactions. During storm onset, enhanced electromagnetic ion cyclotron (EMIC) waves are produced near the duskside plasmopause due to injections of ring current ions; these waves tend to produce rapid pitch angle scattering of trapped relativistic electrons, depleting the outer belt on a timescale of hours. Meanwhile, whistler-mode chorus waves are produced by ring current electrons outside the plasmopause from the midnight to dawn sectors. During storm recovery, whistler chorus scatters trapped electrons in both pitch angle and energy, with energy scattering serving to slowly rebuild the outer belt population on a timescale of days. These interactions are summarized in Figure 2.8. Theory and modeling for these processes have been developed to calculate the effect of wave-particle interactions on trapped electrons (Summers and Ma, 2000; Summers et al., 2007a, 2007b). Jordanova and Miyoshi (2005) have modeled the effects of such processes on the ring current and on radiation belt particle populations. The peak EMIC losses are critically dependent on the plasmopause location (Jordanova et al., 2006), which is also a vital separatrix between regions of different loss timescales (Miyoshi et al., 2006). Microbursts of precipitating electrons, representing short bursts of trapped electrons scattered into the loss cone, have been linked to ULF and VLF waves (O'Brien et al., 2003). The ongoing radiation belt modeling efforts would benefit from observations of the plasmasphere and associated plasma waves.

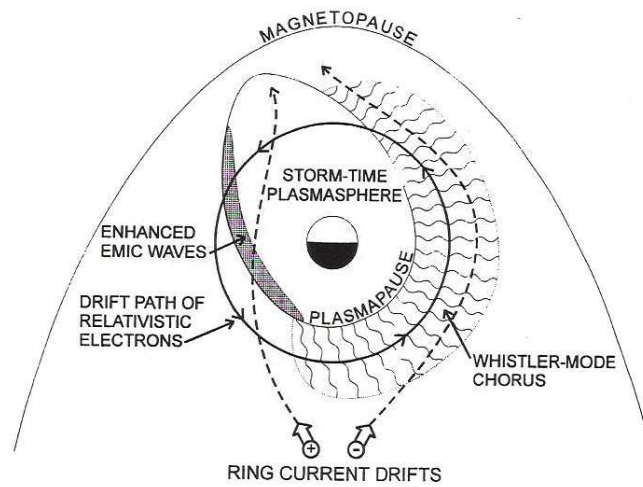


Figure 2.8: Relationship of characteristic wave-particle interaction zones to plasmasphere (from Summers et al., 1998).

# Chapter 3

## Instruments

This project involves space physics instruments on several space platforms, to varying degrees. The main database of plasmopause identifications will be built using DMSP RPA data. The DMSP SSJ/4 instrument provides auxiliary information on the location of the auroral oval. The plasmopause identification method is validated by comparison to IMAGE EUV observations, and then compared to SAMPEX particle instrument observations. The approach for mapping plasmopause locations involves the use of ACE instrument data.

### 3.1 DMSP

**DMSP satellites.** The Defense Meteorological Satellite Program (DMSP) satellites are a series of Air Force satellites with the primary mission of providing weather observations for the Department of Defense. These satellites are in polar sun-synchronous orbits with altitudes near 840 km, orbital periods near 100 minutes, and inclinations near  $99^\circ$ . Table 3.1 gives some data on these satellites. The block 5 satellites have additionally

carried a variety of instruments for space physics observations. This SSIES instrument package for thermal plasma observations was introduced with F8 launched in 1987. With 3 or 4 satellites typically operational at any given time over the last 15 years, these provide a vast dataset of space physics observations. SSIES instruments include: the Retarding Potential Analyzer (RPA), which provides measurements of ion temperature, ion composition, and average ram ion energy relative to the spacecraft; the Ion Drift Meter (IDM); and the SSJ/4 Precipitating Electron and Ion Detectors.

Table 3.1: Information on DMSP satellites carrying SSIES, SSIES-2, and SSIES-3 (from Hairston, 2006, and Anderson, 2007).

satellite	launch date	end of operations	orbital orientation in LT
F8	20 Jun 1987	Jul 1994	0600-1800
F9	3 Feb 1988	Mar 1992	0930-2130
F10	2 Dec 1990	Nov 1997	0740-1940
F11	29 Nov 1991	May 2000	0540-1740
F12	30 Aug 1994	Jul 2002	0830-2030
F13	25 Mar 1995	still operating	0530-1730
F14	4 Apr 1997	still operating	0830-2030
F15	12 Dec 1999	still operating	0910-2110
F16	18 Oct 2003	still operating	0800-2000
F17	4 Nov 2006	still operating	0530-1730

**RPA.** The Retarding Potential Analyzer (RPA) provides data on ion composition, temperature, and velocity in the spacecraft direction of motion (Heelis and Hanson, 1998).

The RPA is basically a shallow cup facing in the direction of spacecraft motion with several successive planar wire grids across the opening. These grids are set at various voltages to permit only ions of a threshold energy (or equivalently, of a threshold velocity) or greater to enter the instrument, where they are observed upon reaching the collector and producing a current. A cross section of the RPA instrument is shown in Figure 3.1. The voltage of the first entrance grid or grid pair (G1) is at sensor ground to avoid affecting particle motion outside the instrument. The last grid, or shield grid (G4), is also grounded to prevent time-varying voltages from producing currents in the collector. Next to the last grid is the suppressor grid (G3), set at a negative potential (e.g. -15 V) to prevent thermal electrons from reaching the collector. A variable positive retarding potential is applied to the second grid or grid pair (G2). This potential determines the minimum energy of ions that are collected. By sweeping a range of retarding potentials, the instrument produces a current versus retarding potential curve, or I-V curve, which contains information on ion composition, density, temperature, and velocity.

For a plasma with no bulk motion relative to the Earth, plasma particles will be incident on the RPA with an inward velocity of order 7.4 km/s (representing the orbital velocity of the DMSP spacecraft). The actual velocities of individual particles will have a thermal distribution about this mean. For a plasma temperature of 1200 K, the associated mean thermal speeds (from  $v = \sqrt{kT/m}$ ) are about 1.1 km/s for O<sup>+</sup> ions, 4.4 km/s for H<sup>+</sup> ions, and 190 km/s for electrons. The incident ions have a Maxwellian distribution about the mean velocity, with a different Maxwellian distribution for different ion species. Figure 3.2 illustrates an ideal current-voltage curve, or I-V curve, from an RPA with a plasma incident at a mean velocity of 7.5 km/s for two choices of temperature. The slope of the I-V curve is related to the Maxwellian distribution and hence to the temperature.

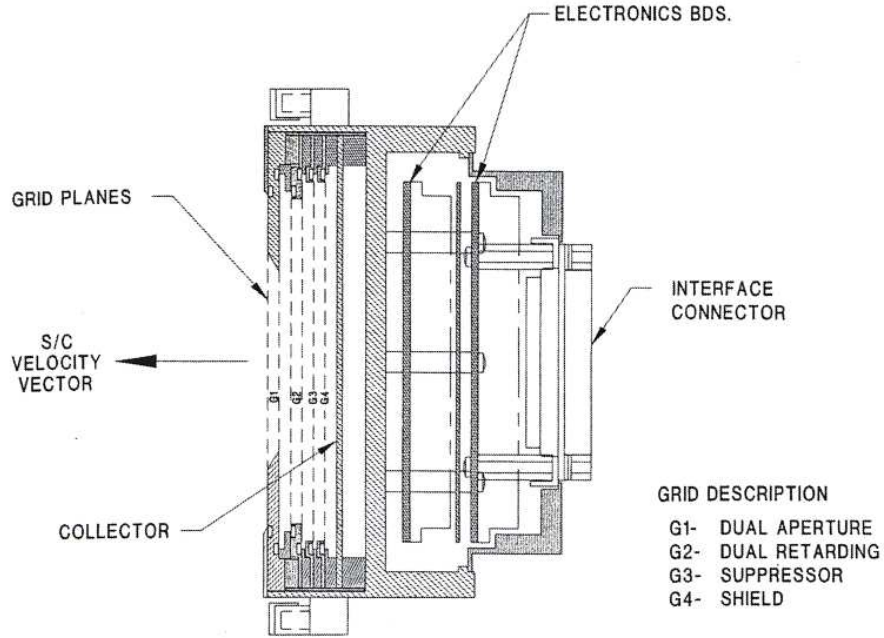


Figure 3.1: Cross section of RPA, showing grids and collector (from Heelis and Hanson, 1998).

The maximum current, at low retarding voltage, scales with the plasma density (with flux through the instrument aperture).

The DMSP RPA sweeps a range of retarding voltages from -3 V to +12 V (alternately sweeping up and down), with the full range covered every 4 s. Routines are used to derive the density of various ions, the ion temperature and relative mean velocity, and the spacecraft potential. Generally, ion species comprising less than a few percent of the total density are difficult or impossible to observe.

**SSJ/4.** The SSJ/4 Precipitating Electron and Ion Detectors provide observations of the flux of precipitating electrons and ions over energies ranging from 30 eV to 30 keV (Hardy et al., 1984). The instrument includes two pairs of electrostatic analyzers, each



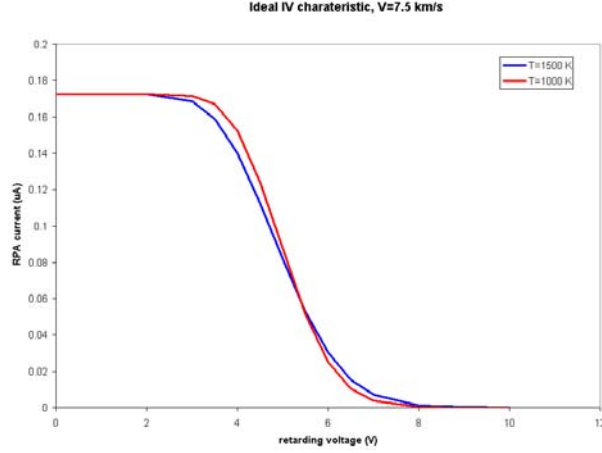


Figure 3.2: Ideal current-voltage curve from an RPA.

analyzer comprising an aperturing system, two concentric cylindrical curved plates, and channeltrons. The plates are set to potentials such that particles of a narrow energy range reach the channeltrons and are detected; the instrument sweeps a range of potentials to obtain flux observations for the range of particle energies, measured in 20 energy channels. The SSJ/4 look direction is towards the zenith. In addition to observing precipitating particles in the auroral zones, the instrument may also observe radiation belt particles. These more energetic particles may penetrate the sides of the instrument and consequently produce a flux versus energy relation generally different than that observed for auroral precipitation.

## 3.2 IMAGE

**IMAGE satellite.** The IMAGE spacecraft was launched 25 March 2000 into an eccentric polar orbit, ranging from 1400 km altitude to 45400 km, or  $8 R_E$ . This orbit allowed

a variety of observations of the inner magnetosphere and the plasmasphere in particular. IMAGE observations considerably advanced observations of plasmasphere dynamics and revealed new degrees of structure. Its instruments included four neutral atom imaging instruments, the Extreme Ultraviolet Imager (EUV), the Far Ultraviolet Imager (FUV), and the Radio Plasma Imager (RPI). The spacecraft ceased operating 18 December 2005.

**EUV imagers.** The three EUV imagers, with overlapping fields of view, are sensitive to the 30.4 nm sunlight scattered by  $\text{He}^+$  (Sandel et al., 2000). Since the plasmasphere is about 5-10%  $\text{He}^+$ , this permits direct imaging of the plasmasphere when IMAGE is near apogee. Each sensor has a  $30^\circ$  field of view, with relative offsets of  $27^\circ$  between successive sensors. The individual sensors use a combination of multilayer mirrors and filters to provide high transmission of 30.4 nm EUV while excluding as much as possible other emissions such as the hydrogen Lyman- $\alpha$ . Spacecraft rotation permits observation of an  $87^\circ$ -wide swath across the sky each rotation. EUV images are obtained at 10 minute intervals. Using such images when apogee occurs well above or below the equatorial plane, the images from the three detectors may be combined into a single image. For applications such as analysis of the plasmopause this is frequently reprojected into a desired frame of reference. Typically, the EUV imagers are able to detect regions of the plasmasphere where  $\text{He}^+$  densities are at least  $\sim 40 \text{ cm}^{-3}$  (Goldstein and Sandel, 2005).

### 3.3 SAMPEX

**SAMPEX satellite.** The Solar, Anomalous, and Magnetospheric Particle Explorer (SAMPEX) satellite was designed to observe energetic electrons and ions in low-Earth orbit. It was launched 3 July 1992 into an orbit of 520-670 km altitude with an  $82^\circ$

inclination and is still operational. Its four particle instruments include the Low Energy Ion Composition Analyzer (LEICA), the Heavy Ion Large Telescope (HILT), the Mass Spectrometer (MAST), and the Proton/Electron Telescope (PET) (Baker et al., 1993). While in a low-Earth orbit, the high inclination of SAMPEX cuts across high  $L$  shells and permits observation of radiation belt particles that mirror at or below the SAMPEX orbit altitude. The spacecraft maintains an orientation such that the instruments point towards the zenith while over the poles, and parallel to the equator when crossing the equatorial plane.

**PET.** In particular the PET measures electrons of energy 0.4-30 MeV and protons or helium nuclei of energy 18-250 MeV (Cook et al., 1993). The instrument has an aperture of  $58^\circ$  and uses eight successive solid state detector surfaces, as shown in Figure 3.3. The first two surfaces are curved to collimate incoming ions for a range of incident angles. The six flat detectors each include a central area to measure energy loss of transiting particles and an outer annular guard region which detects particles entering or leaving the sides of the telescope. A thin aluminized-Mylar sheet at the front aperture provides electrical and sunlight shielding for the detectors. The PET uses a variety of analysis modes which in general register an incident energetic particle by a coincident detection in several detectors. Cumulative counts are recorded in 6 second intervals, and in addition the front detector is sampled for 0.05 seconds of every 0.10 seconds to provide fast time scale counts of magnetospheric particles (energies  $> 0.4$  MeV for electrons,  $> 4$  MeV for protons). This mode facilitates observations of short duration microbursts of precipitating electrons, discussed by Nakamura et al. (2000).

The observed flux of energetic particles along the orbital path of SAMPEX is used to derive flux as functions of time,  $L$  shell, and energy level. The result is a long term database

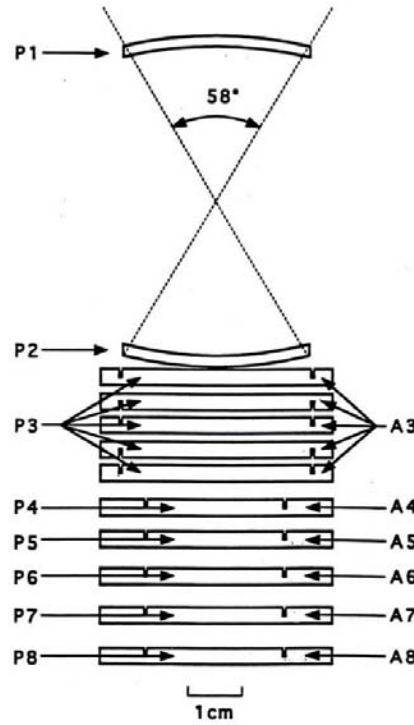


Figure 3.3: Diagram of SAMPEX Proton/Electron Telescope detector surfaces (from Mewaldt, 1993).

of radiation belt dynamics. Figure 3.4 illustrates the type of data available, showing a spectrogram of energetic electron observations for an eight-year period. Significant changes in the outer electron belt, both in number flux and radial location, are visible.

Although the instruments do not provide pitch angle information with normal spacecraft orientation, the spacecraft has been occasionally placed in a spin mode to enable such data collection. In this mode the spacecraft rotates about the Sun-pointing axis at 1 rpm. This provides measurements over all pitch angles twice per revolution. The spin mode has been used during periods from 1996 to 1998, plus several shorter intervals since then, as listed in Table 3.2.

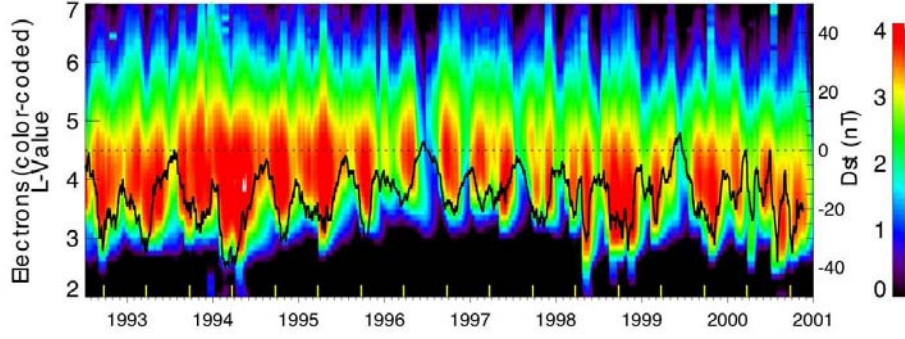


Figure 3.4: SAMPEX observations of 2-6 MeV electrons from 1992 to 2001. Scale for electron flux shows logarithm of number per  $\text{cm}^2\text{-s-sr}$ , in bins of  $0.1 L$  and 30 days. Black line shows Dst (from Li et al., 2001).

### 3.4 ACE

**ACE spacecraft and instruments.** The Advanced Composition Explorer (ACE) spacecraft was launched 25 August 1997 to observe solar wind and energetic particles from outside the Earth’s magnetosphere (Stone et al., 1998). It is located in the L1 libration point,  $1.5 \times 10^6$  km from the Earth towards the Sun, and has operated on station there from December 1997 to the present. Of its six instruments for observing ions of varying masses and energies, the Solar Wind Electron Proton Alpha Monitor (SWEPAM) provides key solar wind parameters. SWEPAM includes two instruments, the SWEPAM-I and SWEPAM-E for observations of ions ( $\text{H}^+$  and  $\text{He}^+$ , specifically) and electrons, respectively (Margolies and von Rosenvinge, 1998; McComas et al., 1998). Each provides data on density, temperature, and three-dimensional bulk flow for the target species. Both are essentially spherical section electrostatic analyzers, with a narrow aperture passing charged particles between two charged analyzer plates, such that particles within a narrow energy

Table 3.2: Spin mode periods for SAMPEX (from SAMPEX Data Center, 2007).

start time	date	end time	date
1507	1 Feb 1996	1915	1 Feb 1996
1334	13 Feb 1996	1930	14 Feb 1996
2030	14 Feb 1996	1800	16 Feb 1996
1525	5 Mar 1996	1745	8 Mar 1996
1333	8 May 1996	0000	19 Aug 1996
0853	26 Aug 1996	1326	6 Nov 1997
1226	17 Nov 1997	1308	18 Dec 1997
1245	14 Jan 1998	1508	21 Apr 1998
1608	28 Apr 1998	1505	7 May 1998
2010	17 Dec 1999	2020	25 Dec 1999
2330	28 Dec 1999	2005	2 Feb 2000

range are passed to a series of channel multipliers. The series of multipliers (16 each), combined with the off-axis rotation of the entire spacecraft, permit the derivation of the directional distribution for the incident particles. The analyzer plate voltage is swept to sample a range of energy values with a cadence of 64 seconds. The SWEPAM-I observes an energy range of 260 eV/ $q$  to 36 keV/ $q$  (for ion charge  $q$ ) and the SWEPAM-E a range of 1.6 eV to 1.35 keV. Measurements of the strength and direction of the IMF are provided by the Magnetic Fields Experiment (MAG) (Smith et al., 1998). The instrument includes two boom-mounted triaxial magnetometers each located 4.19 m from the center of the spacecraft.

**Solar wind data.** Data from SWEPAM, combined with data from other ACE instruments, are used to provide near-real time data on the solar wind (Davis et al., 2007). Verified data include three-dimensional components of IMF;  $H^+$  density, temperature, and three-dimensional velocity; and the  $He^+/H^+$  ratio. From this plasma data the solar wind pressure (dynamic) may be obtained:

$$P = m_p[H^+] \left( 1 + 4 \frac{[He^+]}{[H^+]} \right) V^2 \quad (3.1)$$

where  $m_p$  is the mass of the proton and  $V$  is the solar wind velocity.

For application to magnetospheric modeling, ACE data must be propagated to the magnetopause. Observations by ACE are made at  $\sim 240R_E$  sunward, and with a typical solar wind velocity of 400 km/s these conditions take on the order of an hour to reach the Earth's magnetopause. In general the solar wind direction is not parallel to the Earth-ACE line; additionally, IMF variations may propagate as planar structures which are not aligned with the solar wind direction. Techniques for propagating observed solar wind and IMF parameters to the magnetopause have been described (Weimer et al., 2003), and some data sets are available incorporating these corrections (e.g. Weygand, 2007). Such solar wind/IMF parameter data sets provide input to magnetospheric magnetic field models such as the Tsyganenko 2001 model (Tsyganenko and Sitnov, 2005).

# Chapter 4

## Method and Initial Results

One of the best ionospheric signatures of the plasmopause has been proposed to be the LIT, which can be identified from DMSP RPA observations. Further, the temporal coverage by multiple DMSP satellites provides a large database of potential observations. These facts enable our approach, which is to develop a process for extracting an LIT-based plasmopause identification from DMSP observations and map these locations to the equatorial plasmopause. These results are compared to other plasmopause observations such as those from IMAGE. Once validated, an extended database of DMSP plasmopause locations will be compared to SAMPEX observations to test the plasmopause-radiation belt relationship.

In the following discussion of our approach, we will refer to results from two initial case studies. The first is a one-day study, using observations from 18 June 2001 (day 169). The second is a 72-day study, covering 21 March-31 May 2001 (days 80-151). These periods were selected because IMAGE observations were available for these periods for comparison. These results are also summarized in Anderson et al. (2007).



## 4.1 LIT identification

Observations from the DMSP RPA can identify the LIT, described in the literature as one of the best ionospheric signatures of the plasmapause. We use RPA observations of  $H^+$  density to identify the LIT. The RPA also provides observations of  $He^+$  density, which can be used in principle; however, the lower helium abundances result in relatively noisy data which prove less useful for identifications.

Ideally, the LIT in  $H^+$  density is characterized by a sharp gradient, dropping from higher densities equatorward to the lower densities characteristic of the auroral zone and polar cap. After investigating several alternatives, we have adopted the density minimum on the poleward side of this gradient as proxy for the plasmapause. In comparisons to IMAGE data (described in the next section), identifications centered on the gradient region were often significantly equatorward of the high altitude plasmapause.

Generally, each DMSP satellite crosses the equatorward auroral zone boundary four times per orbit. This gives an average of about 58 crossings per day. Assuming three satellites in operation, this is potentially over 63,000 crossings per year. However, the LIT is generally only observable by DMSP when the  $O^+$  transition height is below DMSP altitude ( $\sim 840$  km), generally requiring that the satellite be in darkness (there are additional seasonal/solar cycle variables). Still, this gives a potentially large database.

The current procedure for boundary identification is as follows, with numbers [1-7] referring to elements in Figure 4.1. The DMSP observations of  $H^+$  density [1] are obtained from the UTD processed data with a cadence of 4 s. For each DMSP pass, we take an  $N$ -point smooth of the  $H^+$  density data from between  $20^\circ$  and  $65^\circ$  magnetic latitude [2]. If the dynamic range [3] of the resulting series is less than a factor of  $\beta$ , the pass is

automatically rejected; some remaining passes are also manually rejected at this point on the basis of factors such as very noisy data or no evident LIT (as is often the case for dayside passes). For each pass that is analyzed, a range of MLAT near the LIT density minimum is manually specified [4], and the routine identifies the density minimum in this range [5]. Proceeding equatorward from this minimum, the LIT boundary is selected as that point [6] where the smoothed density reaches a value a factor of  $f$  greater than the density value at the identified minimum. The values of  $\beta$ ,  $N$ , and  $f$  are free parameters; the current implementation of the algorithm uses  $\beta = 10$ ,  $N = 5$  and  $f = 1.5$ . A boundary is also manually selected [7] at the poleward side of the LIT gradient, where the slope of the gradient drops to a low value and before the noisy density data associated with the auroral zone/polar cap begin. If the location selected by the routine [6] is separated from this manually-selected boundary [7] by more than  $2^\circ$  in magnetic latitude or otherwise discordant (i.e. if noise in the data warranted rejection at an earlier stage), it is rejected. Table 4.1 presents figures on the culling of passes in this process for the 72-day study period, using data from F12, F13, F14, and F15.

Table 4.1: Culling of passes for plasmopause identifications, 72-day study period.

stage	number of passes
all passes in 72 days	14,894 (100%)
rejected by program	8,286 (55.6%)
rejected manually before analysis	4,631 (31.1%)
rejected manually after analysis	187 (1.3%)
retained in database	1,790 (12.0%)

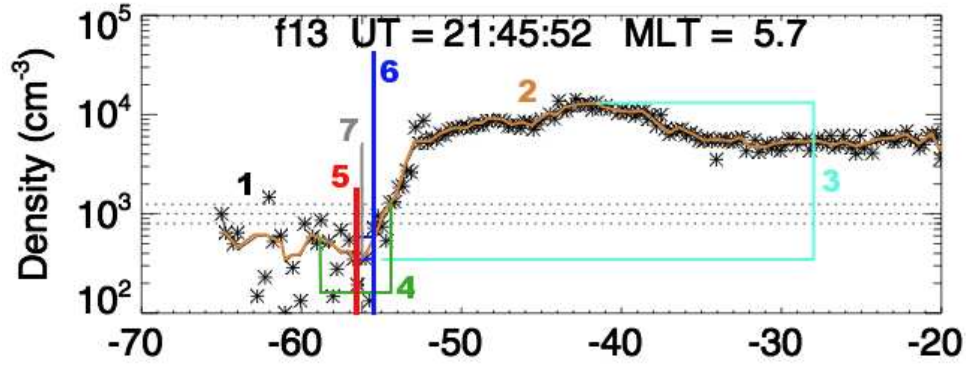


Figure 4.1: Illustration of method for identifying the LIT, with stages [1-7] as explained in the text.

Figure 4.2 shows a sequence of DMSP observations during an active period. Each plot shows  $H^+$  density (measurements as asterisks with 5-point smoothed line in red). The vertical blue line shows the plasmapause location as identified from the LIT as described above. The vertical red line is the equatorward electron precipitation boundary as identified from DMSP SSJ/4 observations; note that the plasmapause is equatorward of the precipitation boundary in all cases, as expected. The sequence shows evolution of the ionospheric signatures of the plasmasphere during a geomagnetic storm: initial high latitude/radial location of the plasmapause (a); equatorward/earthward movement of the plasmapause during stormtime erosion (b); and an eroded plasmasphere with a sharp low latitude/altitude plasmapause (c), with refilling to pre-storm plasmaspheric extent taking days.

Applying our method to the 72-day study period, we have obtained 1790 plasmapause identifications or an average of 25 identifications per day. The number of identifications per day varied from 0 to 47, as summarized in Table 4.2:

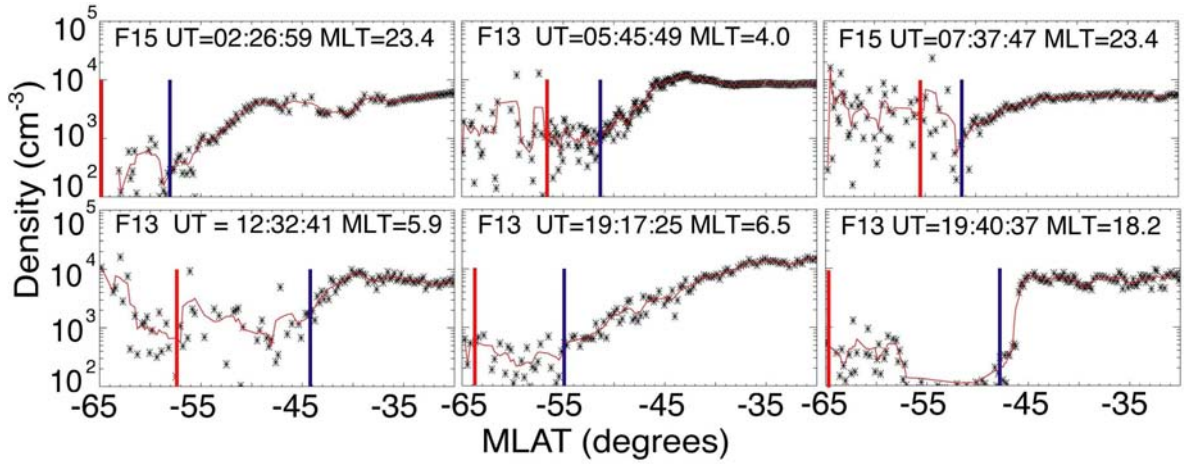


Figure 4.2: Sample DMSP observations of  $H^+$  density versus magnetic latitude (asterisks) with smoothed fit (narrow red line). Vertical lines show electron precipitation boundary (red) and identified LIT/plasmapause (blue).

Table 4.2: Distribution of number of plasmapause identifications per day, 72-day study period.

IDs per day	number of days
0	1
1-10	4
11-20	19
21-30	27
31-40	16
41-47	5

We have examined different algorithms for identifying the plasmopause based on the LIT. Our first approach used a log-linear fit to the density gradient in  $H^+$  density and identified where this fit crosses a threshold (e.g.  $10^3 \text{ cm}^{-3}$ ). This method, while potentially easier to automate, tended to produce plasmopause identifications significantly equatorward of locations in IMAGE observations. Better results have been obtained using the density minimum approach, as will be shown.

## 4.2 Mapping to plasmasphere

The DMSP-identified plasmopause locations are at low altitude; to identify these with the high altitude plasmopause, these satellite locations must be mapped along magnetic field lines to the equatorial plasmopause (or any other desired high altitude location). Since the equatorial plasmopause is distant enough for the geomagnetic field lines to be stretched, such mapping must include the effects of both the internal geomagnetic field and the external magnetic field associated with the influence of the Sun on the magnetosphere.

Currently our mapping uses the IGRF 2000 internal magnetic field model with the Tsyganenko 2001 external magnetic field model (Tsyganenko and Sitnov, 2005). Both are available in GEOPAK routine package, implemented in FORTRAN. We use a FORTRAN code as a driver to call the appropriate routines, including both internal and external field models. The code has an option to use the internal field only, which can be used for appropriate comparison to databases that use only an internal field.

The Tsyganenko 2001 model requires as input the solar wind pressure, IMF  $B_Y$  and  $B_Z$ , and Dst. The Dst values are obtained from the WDC for Geomagnetism, Kyoto (2007). The solar wind and IMF data are available from the ACE data center (Davis et al., 2007)

with a 1-hour time resolution, propagated to the magnetopause. However, during active times the timescale for magnetospheric changes may be much shorter. ACE Level 2 data with a resolution of 64 s includes solar wind velocity,  $H^+$  density, ratio of  $He^+$  to  $H^+$ , and IMF  $B_Y$  and  $B_Z$ . This data includes data gaps and is unpropagated. For the one-day study, we have used the ACE Level 2 data to obtain high resolution model parameters by extrapolating to fill data gaps, calculating solar wind pressure, and propagating the data from ACE to the Earth's location by projecting the solar wind velocity vector onto the ACE-Earth displacement vector. These results do not include corrections available in more properly propagated data sets, but available data sets contain significant gaps. The process to produce high-resolution model parameters has been partially automated; this will be more fully automated for use in the project.

Given the appropriate model parameters, the driver code uses GEOPAK routines to trace the magnetic field line through a specified satellite location, in both directions along the field line. The traced field line is then used to obtain the field line intersection with equatorial planes in various coordinate systems (SM, GSM, geographic, and magnetic); the radial location of the maximum extent of the field line (associated with apex coordinates); the magnetic local time and latitude; and dipole L value. GEOPAK is designed for tracing field lines in the extended magnetopause and consequently has a larger step size than other line tracing programs; consequently, the accuracy for MLT and MLAT is relatively poor, e.g. of order  $0.2^\circ$  for MLAT.

The processing of the RPA data strictly identifies the plasmopause crossings by UT of observation. Associating this with a particular location in space is dependent on the ephemeris data. However, the ephemeris data within the DMSP data files may be in error by several tenths of a degree due to use of orbit calculations incorrectly account-

ing for satellite drag and other effects. Phil Anderson has recently compiled a database of ephemeris positions for the DMSP satellites at 10 s intervals using accurate orbital propagation; this ephemeris data will be used from now on.

Due to the constraints associated with the  $O^+$  transition height and the sun-synchronous DMSP orbits, passes where the LIT is observable are generally limited to winter dawn or dusk passes for F8, F10, F11, and F13, and to winter pre-dawn passes for F9, F12, F14, and F15. As such locations are mapped to high altitude field lines, these lines are generally swept anti-sunward. In addition, the sun-synchronous DMSP orbits limits observations to a particular range of MLT for each satellite. Together, these constraints result in most of our plasmopause identifications being in a limited range of MLT. For the 72-day study period, most of the plasmopause identifications are from dusk to midnight (MLT of 1700 to 0100) or predawn to dawn (MLT of 0300 to 0700), as shown in Figure 4.3 (note that these MLT figures refer to the high altitude location).

In addition to mapping the database of plasmopause locations using the FORTRAN code, we have also mapped all satellite positions at 10 s intervals to corresponding high altitude locations for several days. Using such datasets, the orbit track of DMSP may be represented as its high altitude magnetic projection. This has been used for studies of subsets of passes as in the next section.

O'Brien and Moldwin (2003) developed empirical plasmopause models, including one parameterized by both Dst and MLT. For the 1790 plasmopause identifications from the 72-day case study, we have calculated plasmopause  $L$  values from the O'Brien-Moldwin model, using the mapped MLT for each identification. Figure 4.4 shows a comparison of the DMSP observations and model results, with O'Brien-Moldwin model  $L$  values plotted versus DMSP-derived  $L$  values. For DMSP-derived  $L$  values of 2 to 4, the model plasma-

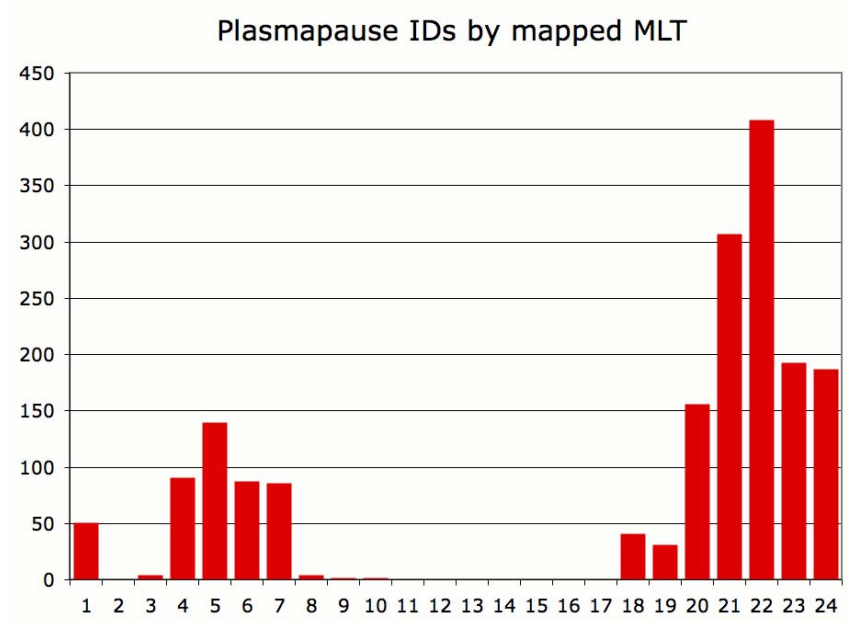


Figure 4.3: Number of plasmapause identifications by MLT for the 72-day study period (2001 days 80-151).

pause  $L$  value tends to be greater by about 1. The larger mismatch for model  $L$  values greater than 5 may represent a breakdown in the model or the DMSP method capabilities or both. The nature of the model parameterization may introduce a bias for Dst values near 0, corresponding to extended plasmasphere conditions. The discrete values of model  $L$  values near  $L = 6$  and  $L = 6.5$ , specifically, result from discontinuities from rounded Dst values. At the same time, our DMSP-based approach may have difficulty extracting plasmapause locations when the plasmasphere is extended and diffuse.



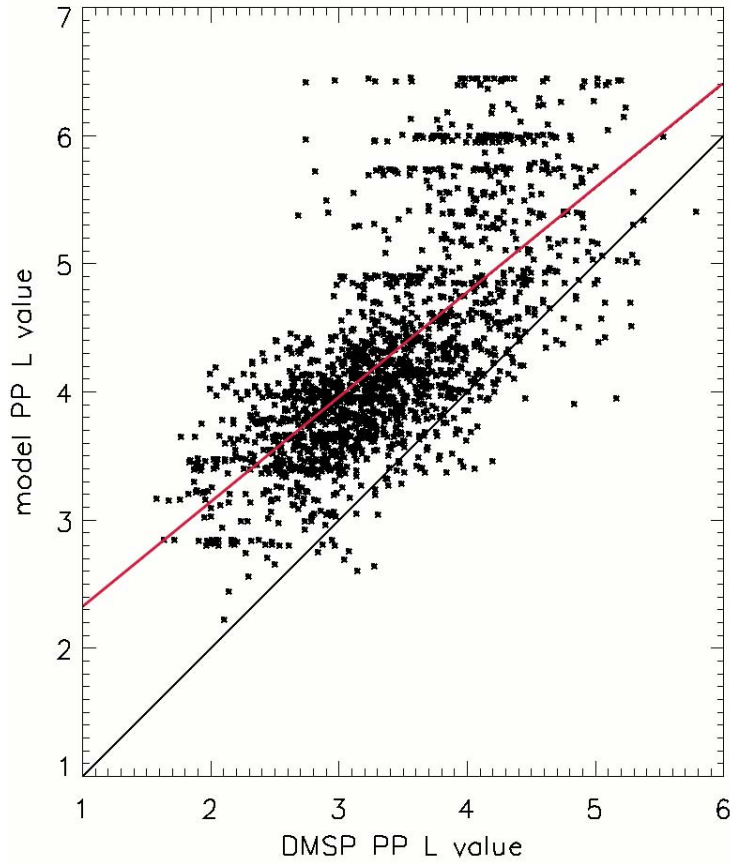


Figure 4.4: Comparison of O’Brien-Moldwin model plasmopause locations to DMSP plasmopause observations for the 72-day study period (2001 days 80-151). Red line indicates best linear fit to comparisons, black line indicates identical plasmopause  $L$  values.

### 4.3 Comparison to IMAGE observations

IMAGE EUV observations are unique in providing a global picture of the structure of the plasmasphere. Such observations suffer some limitations: they are only available for those periods when IMAGE was both near apogee and at high latitude (conditions met on some orbits but not others due to precession of the orbit); and they must be appropriately

reprojected from the observed plane to the desired frame of reference.

Jerry Goldstein has developed several databases of processed IMAGE data. His analysis method involves projecting each pixel of an IMAGE image to the maximum  $L$ -shell it intercepts, and mapping these results to either  $L$  and MLT or to the SM equatorial plane. The resulting image is used to manually extract the plasmopause location as a set of points. The periods for our two initial case studies were selected to coincide with periods where Goldstein has produced processed IMAGE datasets (reprojected images and/or datasets of plasmopause extractions). This permits comparison of our DMSP-based plasmopause identifications to the plasmopause identified by IMAGE.

Figure 4.5 shows results for the one day study (18 June 2001) from mapping DMSP-identified plasmapauses in comparison to IMAGE observations. IMAGE EUV observations are shown projected to the SM  $X - Y$  plane (see Goldstein and Sandel, 2005), with the Sun at right. Red lines show DMSP orbit tracks mapped along field lines to this plane, with the extracted plasmapauses indicated by red crosses. The plotted passes show all plasmopause identifications from F12 through F15 that were within 30 minutes UT of an available IMAGE observation. In nearly all cases the DMSP and IMAGE plasmopause agree within a fraction of an  $L$  value, including cases where structure is present such as images for 1803 and 1945. In the case with the largest disagreement, a premidnight pass near 1407, the DMSP plasmopause is noticeably inward of the IMAGE plasmopause.

For the 72-day case study we have made quantitative comparisons of the DMSP and IMAGE plasmopause identifications. Goldstein has extracted partial plasmopause boundaries, generally covering the night side from dusk to dawn, from 1547 IMAGE EUV observations for days 89 to 149 of 2001. We identified all DMSP plasmopause identifications coincident with an extraction set in the Goldstein set, i.e. within 15 minutes of UT, and

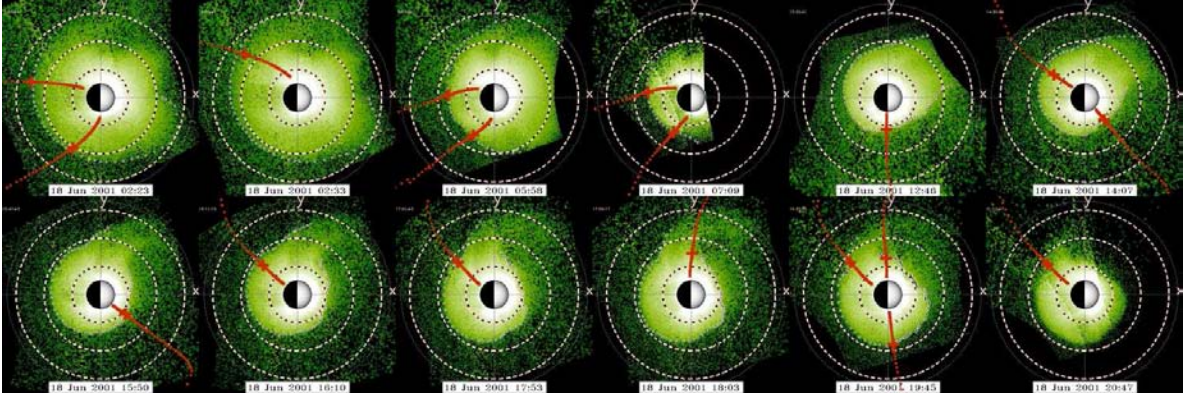


Figure 4.5: Comparison of IMAGE EUV observations of plasmasphere to DMSP-extracted plasmopause locations, both mapped to SM  $X - Y$  plane. Sun is to the right, dawn to top. Red traces indicate mapping of DMSP orbit paths, with plasmopause identification as red crosses.

derived an IMAGE-based  $L$  value by averaging the IMAGE plasmopause points within 15 minutes of MLT of the DMSP identification. This provided 187 comparisons, which are shown in Figure 4.6. The comparisons fall in two clusters: one of good matches ( $N=147$ , 79% of sample) with a mean difference in  $L$  value of  $0.451 \pm 0.428$ ; and a second of mismatches ( $N=40$ , 21% of sample) with a mean difference in  $L$  value of  $1.784 \pm 0.451$ . Most of the sample then is in the cluster where the DMSP plasmopause is on average  $0.5 L$  inward of the IMAGE plasmopause. Given that the error in the IMAGE-extracted plasmopause is  $\sim 0.2 L$ , this difference is not unreasonable.

However, the mismatch cluster represents a significant difference and so we have examined this cluster to look for any systematic explanation. We have variously examined the DMSP LIT density profiles, the relevant raw (not reprojected) EUV images, and mappings of DMSP orbit tracks. Based on this review, most of these cases appear to involve high

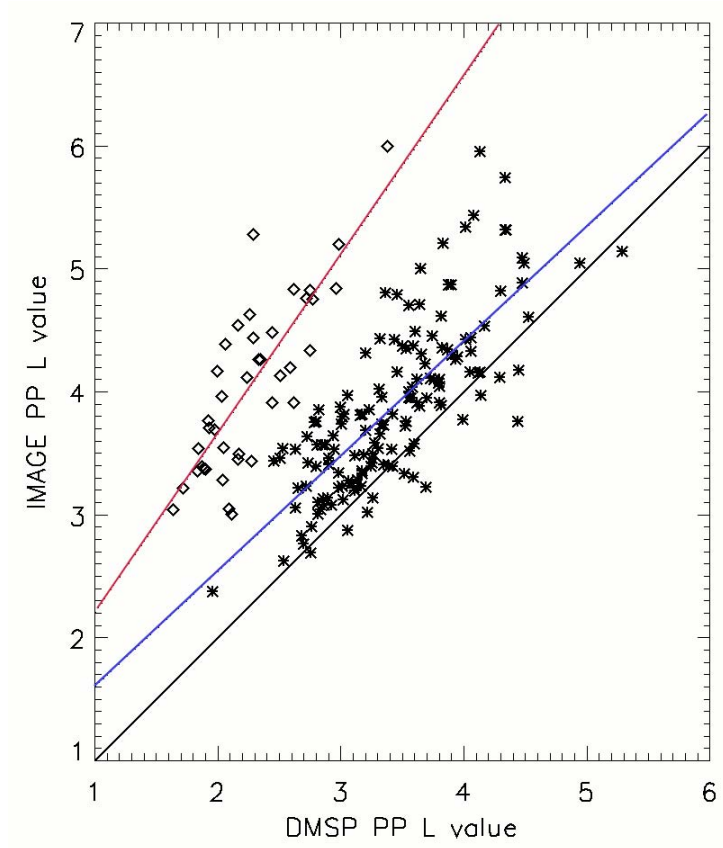


Figure 4.6: IMAGE-identified plasmopause  $L$  value versus DMSP-identified plasmopause  $L$  value. Lines indicate best linear fit for good match cluster (blue) and mismatch cluster (red) and identical plasmopause  $L$  values (black).

levels of plasmopause structure possibly not represented in the IMAGE-based dataset. The available raw EUV images suggest that a number of cases involve plasmasphere density structures within the outer threshold-based plasmopause identified in the IMAGE extractions. Table 4.3 summarizes the review of these cases. Half of the cluster is in three sets of identifications, each in a few hour period on days 91, 92, and 101. For these cases the raw images suggest the possibility of plasmasphere density structures or irregu-

larities, but this determination is inconclusive pending examination of processed IMAGE observations. For nine passes on days 128-137, the EUV images show plumes or other structure, and correspondingly the DMSP mismatch passes are nearly coincident in time with good matches. Two cases on day 113 were counted as mismatches simply because of the averaging of IMAGE  $L$  values across a plume.

Table 4.3: Summary of mismatch cases, 72-day study period.

mismatches, day (total cases)	notes on IMAGE data	notes on DMSP data
91 (5)	possible plume	possible plume in two passes
92 (9)	possible structure	
101 (6)	possible structure	
102 (2)	possible plume	
103/112/147 (3)		possible bad ID
113 (3)	plume	match to plume
119 (1)	plume	
128/132 (4)	structure	near-coincident matches
129/133 (4)	plume	near-coincident matches
137 (1)	diffuse boundary	near-coincident match
149 (2)	notch	notch evident

Several passes from days 101 and 149 bear scrutiny because the DMSP data clearly show plasmaspheric density structures. For two of the mismatches on 101, plus one good match, the DMSP data strongly suggest a plume or other structure. Figure 4.7 shows

DMSP  $H^+$  density profiles for a good match (top) and the two mismatches (middle and bottom). All three show a high latitude density increase above the apparent LIT, but below the latitude of noisy auroral zone data. In the good match, the boundary was selected on the outside of the plume, whereas in both mismatch cases it was selected inside the plume. Similarly, the two mismatches on 149 apparently involve a plume based on examination of IMAGE and DMSP data. Figure 4.8 shows DMSP  $H^+$  density profiles for three passes: the first (1051) and third (1233) are mismatches, while the second (1229) is one of two good matches nearly coincident in time and MLT. The corresponding IMAGE EUV raw image shows a notch in the pre-midnight sector. The mapped DMSP orbit track for the first pass (1051) differs from the other passes in that it crosses a wide range in MLT in the outer plasmapause. This would explain why this density profile shows structure, possibly from both sides of the notch. It appears that the 1233 mismatch was inside the notch, at MLT=21.0, while the 1229 good match at MLT=21.9 and a similar good match at 1245 UT and MLT=19.9, were outside the notch on either side. Examination of the mismatch cluster thus suggests that our DMSP-based plasmapause identifications are likely identifying physical structures in the plasmasphere, even in these cases of apparent disagreement with IMAGE.

## 4.4 Comparison to SAMPEX observations

After completing the method for extracting the plasmapause location and applying it to the DMSP database, we expect to have several years' worth of data to compare to SAMPEX observations of radiation belt particle populations. We have made two types of preliminary comparisons to illustrate the types of investigations we will undertake. The

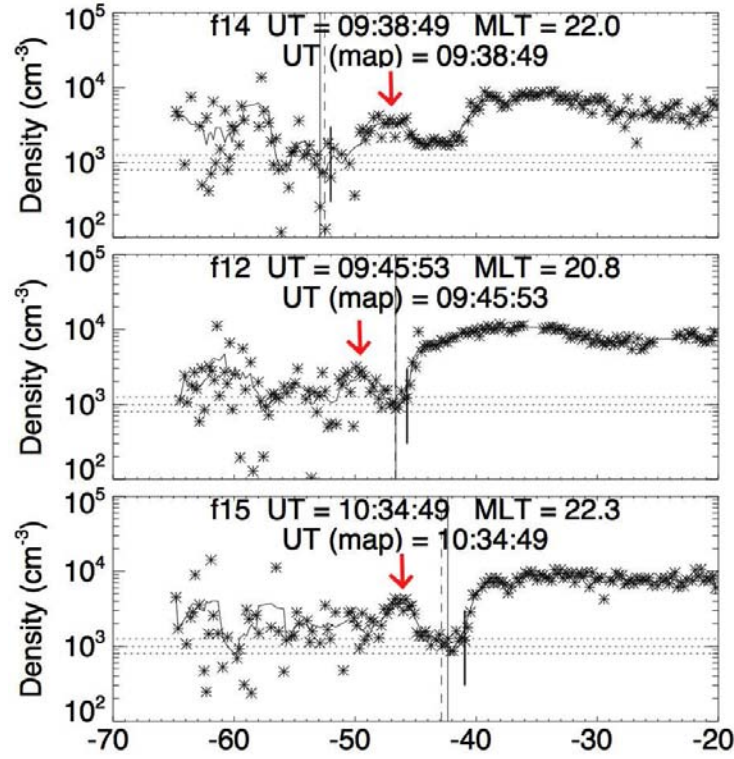


Figure 4.7: DMSP  $H^+$  density observations on three passes, day 101; one good pass (top) and two mismatches (middle and bottom). Red arrows indicate apparent plume-like structures.

first is shown in Figure 4.9, covering the 72-day study period in 2001 (overlaid on a figure from Goldstein et al., 2005b). The top figure shows DMSP-identified plasmopause locations (black) compared to IMAGE-identified plasmopause locations in color. For the IMAGE-based locations, note that each IMAGE observation was used to produce a series of plasmopause extractions covering (generally) the night side; each blue dot represents the average of a series from a single image, and each red dot the minimum  $L$  value in a series from one image. All available DMSP-identified locations are shown, and as discussed



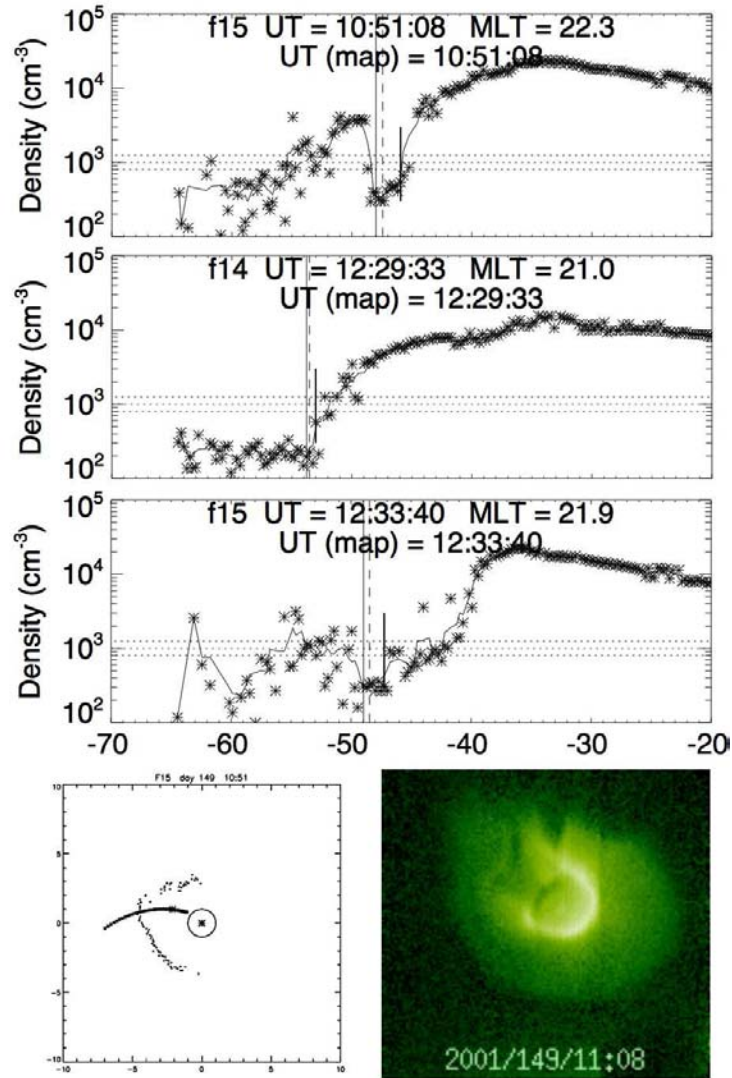


Figure 4.8: DMSP  $H^+$  density observations on three passes, day 149: mismatch with apparent structure (top), good match (second), and mismatch (third); DMSP orbit track in SM equatorial plane for first pass (bottom left); and corresponding IMAGE EUV raw image (bottom right).



previously these tend to represent limited ranges of MLT (dusk to midnight or predawn to dawn). The DMSP identifications correlated well with the IMAGE identifications, and this plot particularly illustrates the ability to fill in gaps in IMAGE coverage with the DMSP-based approach. The middle panel shows daily averages of SAMPEX electron counts (2-6 MeV range) with the daily average DMSP-derived plasmopause location (white line). The bottom panel shows Dst index. Several disturbances (indicated by vertical black lines) are each accompanied by a prompt depletion of the outer belt electron population followed by repopulation over several days. The plasmopause moves inward with each disturbance, moving outward gradually during several days' refilling. Our plasmopause observations show a correlation with outer radiation belt behavior, like that observed by Goldstein et al. (2005b). Specifically, for most disturbances the rapid inward movement of the plasmopause correlates with rapid depletion of the outer radiation belt followed by recovery at a more inward location; conversely, as the plasmasphere slowly refills and expands, the outer radiation belt tends to migrate outward. Disturbance 4 is a counterexample to this correlation: the outer radiation belt is depleted and recovers, but without radial migration. Addressing such questions may involve more than merely correlating dynamical trends, but using the DMSP and SAMPEX data to address the specific issues of particle source and loss regions.

The second preliminary comparison to SAMPEX data is one example. Figure 4.10 shows the DMSP-based plasmopause identifications for the 72-day study in black, while the red points show the location of SAMPEX-identified microbursts of precipitating electrons. These microbursts have been shown by O'Brien et al. (2003) to be associated with the presence of plasma waves that likely serve to scatter trapped particles into the loss cone, where they are then observed by SAMPEX. Note that the locations of microbursts, with

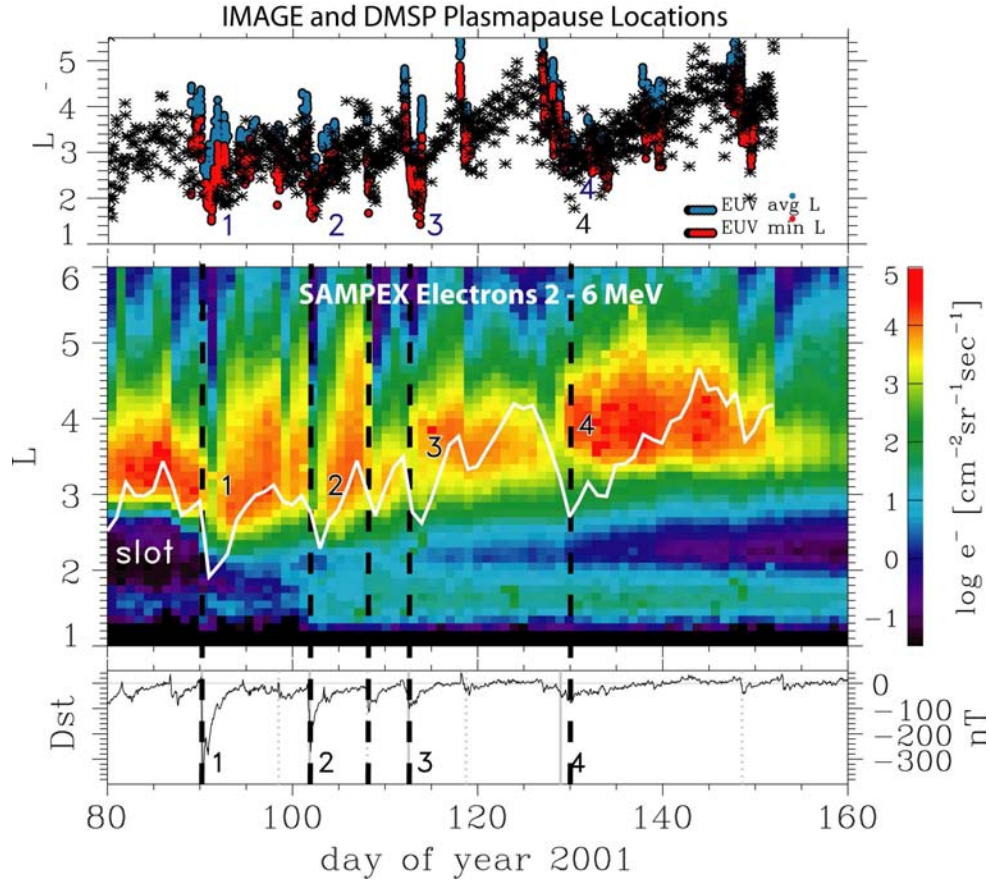


Figure 4.9: Comparison of plasmopause locations and radiation belt observations: top, plasmopause locations from DMSP (black) and IMAGE (average in blue, minimum in red, from each EUV mosaic); middle, daily average SAMPEX electron counts in 2-6 MeV range and daily average DMSP-identified plasma-pause (white line); bottom, Dst index. Vertical dashed lines indicate major disturbances.

very few exceptions, are outside the range of  $L$  values identified by DMSP. Nonetheless, the two groups track consistently: inward movement of the plasmopause is accompanied by inward movement of microbursts, and they both move outward slowly during recovery.

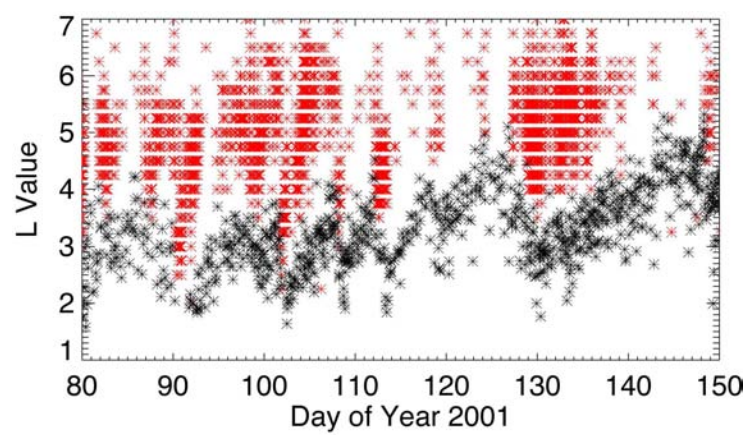


Figure 4.10: Comparison of DMSP-identified plasmopause locations (black) to  $L$  values of relativistic microbursts (red) identified by SAMPEX.

# Chapter 5

## Continuing Research

### 5.1 Planned work

The work to be done includes refining the LIT identification algorithm, particularly to make it more automated; reviewing the source of input parameters for the mapping process; completing comparisons to available IMAGE data and possibly POLAR data; completing the database; and conducting case studies and statistical studies in concert with SAMPEX data.

To facilitate applying the LIT identification method to the full DMSP dataset, as well as reduce the subjective elements, it is desirable to make the procedure more automated. Several approaches have been examined: using the change in variance in the data to identify when the “noisy” polar cap data is encountered; calculating a running linear fit to several points at a time, to identify where the LIT gradient occurs. Neither of these has produced satisfactory results thus far: since the level of noise in the data is highly variable, both from one satellite to another and for various conditions for a given satellite,

establishing a fixed criteria based on variance and/or gradient has been elusive. A gradient-based criterion, i.e. based on the slope of the gradient, may still be useful to describe as a quality flag or to classify the type of boundary observed. Such a criterion may permit elimination of some questionable cases, given that the potential database is large enough to withstand additional culling. However, any such criterion must be selected so as not to introduce a bias in the sample. For this reason we have been careful about making rejections based on slope (i.e. low gradient in density) to avoid biasing the sample against cases with an extended, diffuse plasmasphere. The existing algorithm includes several adjustable parameters. Experiments thus far suggest that parameter values of  $N = 5$  and  $f = 1.5$  yield better results than some alternatives; this issue will be reviewed to optimize the results.

The field line mapping requires solar wind and IMF parameters for input to the external field model. Currently, we have used ACE Level 2 data with appropriate calculations. The process for producing input data will be automated as much as possible. The use of alternate data sources, such as Weygand (2007) will be considered.

We will continue examining the comparisons to IMAGE data. The examination of the DMSP-IMAGE comparison for the 72-day study period is continuing, including comparison to processed EUV images. As we build up the multi-year database, we will make additional comparisons to IMAGE data as the opportunity arises. In addition, we can compare plasmopause identifications by DMSP to those by POLAR at high altitude. While such comparisons will be less frequent, since they require coincident observations by DMSP and POLAR on the same field lines, they will be more direct since POLAR is directly observing plasmaspheric densities in situ.

Our plan is to extract a database of thousands of plasmopause identifications covering

several years of DMSP data. Based on comparison to the 72-day study, the full DMSP database of over 10 years (a full solar cycle) could yield about 100,000 plasmopause identifications. This will then be used in statistical studies with SAMPEX observations to address the plasmasphere-outer radiation belt relationship. Planned or possible components of these studies include: case studies based on epoch analyses; long-term correlation analyses to determine response times for the radiation belt; analyses relating the plasmopause location to scattering of particles into the loss cone; and efforts to place constraints on wave activity affecting radiation belt populations. Stormtime case studies will be possible using first products of the database. These can be used for epoch analyses such as comparative analyses of plasmopause location and outer radiation belt location (characterized by flux) as functions of time from storm onset. Once several years' worth of data are available, we can conduct statistical comparisons to evaluate the timescale for radiation belt response to changes in plasmasphere location. This involves at least two timescales: the time for depletion of the outer belt population, on the order of a day, and the time for repopulation of the outer belt, on the order of several days. The plasmasphere location will be compared to locations where particles are scattered into the loss cone, using both microburst observations and observations of particle distributions versus pitch angle for the periods when this data is available. This will serve to relate such loss events to regions inside or outside the plasmasphere. Finally, use of the plasmopause database to produce a basic assimilative model of the plasmopause location for all MLT, e.g. using the O'Brien-Moldwin model, would permit estimates of the fraction of radiation belt particle orbits spent inside and outside the plasmasphere. This can be compared to observed changes in radiation belt fluxes to examine the possible role of wave-particle interaction in various regions, and perhaps to place constraints on these waves.

## 5.2 Timetable

**Fall 2007:** we will refine the algorithm for extracting plasmopause locations from the DMSP dataset. The procedure for mapping the DMSP-based locations to the plasmopause will be examined in terms of the possible improvement from alternate input datasets (e.g. solar wind parameters). At the same time these results will be tested against all available observations from IMAGE and other datasets as available (e.g. Polar, Cluster).

**Fall 2007-spring 2008:** we will analyze differences between the DMSP identifications and those from IMAGE to determine their cause, e.g. correctable deficiencies in the LIT identification algorithm or the field line mapping. There are differing opinions on whether the LIT corresponds consistently with the plasmopause; we will consider the possibility of limits to conditions where there is a good correlation, e.g. limits in MLT, recent geomagnetic activity, etc. Identification of such limits will constrain the valid regime for the database as well as address the scientific issue of the LIT-plasmopause relationship.

**Spring-summer 2008:** we will perform case studies with comparisons to SAMPEX data during periods of geomagnetic activity. Specifically, we expect that particle populations with orbits passing through the plasmasphere will be depleted due to scattering into the loss cone. This would represent overlap of the plasmasphere into the radiation belt, e.g. through duskside/sunward bulges or plumes. Additionally, we expect slower repopulation of the belts in regions outside the minimum plasmopause  $L$  values. We will analyze these radiation belt changes in comparison to changes in plasmopause location (as described by, e.g., the sample of observed plasmopause locations or in terms of an empirical fit to the observed locations). To more directly address whether the scattering of radiation belt particles is associated with plasmopause location, we will compare our

plasmopause locations to the locations of microbursts of precipitating particles and to locations of particle populations in the loss cone as observed by SAMPEX while it was spinning and thus providing pitch angle information.

**Summer-fall 2008:** we will complete the database from all the available DMSP data. This will permit a statistical analysis over the full database of SAMPEX observations, examining the relationship of the range of plasmopause locations to the location of increased or depleted particle populations. We will quantify the relationship between the LIT and plasmopause, and we will improve physical models for the relationship between the plasmopause location and the outer radiation belt.



# Chapter 6

## Summary and Conclusion

We have demonstrated initial results from a method of identifying the plasmopause in DMSP light ion observations. These observations compare well with IMAGE observations of the plasmopause. Using this method, we expect to produce a multi-year database of plasmopause identifications which we can use to make statistical correlations with outer radiation belt dynamics as observed by SAMPEX, helping to address the question of the role of plasmasphere-related wave-particle interactions in this behavior. We anticipate at least two articles for publication based on this work, possibly one based on the case studies analyzing plasmopause identifications and SAMPEX data and one describing results of long-term statistical analyses or plasmopause location in relation to loss cone populations. The database of plasmasphere observations has many potential applications beyond our use to examine relationship to the radiation belt. The database will be made available to the community, and several researchers have expressed interest in using it in applications such as input to assimilative models of the plasmasphere for radiation belt modeling studies.

# Chapter 7

## List of Acronyms

**ACE** – Advanced Composition Explorer

**AE** – auroral electrojet index

**CRRES** – Combined Release and Radiation Effects Satellite

**DE** – Dynamics Explorer

**DMSP** – Defense Meteorological Satellite Program

**Dst** – disturbance storm-time

**EMIC** – electromagnetic ion cyclotron

**EUV** – extreme ultraviolet

**FAC** – field-aligned currents

**FUV** – far ultraviolet

**GPS** – Global Positioning Satellites

**GSM** – geocentric solar magnetospheric system

**HILT** – Heavy Ion Large Telescope (SAMPEX)

**IDM** – ion drift meter

**IGRF** – International Geomagnetic Reference Field

**IMAGE** – Imager for Magnetopause-to-Aurora Global Exploration

**IMF** – interplanetary magnetic field

**ISIS** – International Satellites for Ionospheric Studies

**ISS** – Ionosphere Sounding Satellite

$K_p$  – *planetarische Kennziffer* (planetary index)

**LEICA** – Low Energy Ion Composition Analyzer (SAMPEX)

**LIT** – light ion trough

**LT** – local time

**MAG** – Magnetic Field Experiment (ACE)

**MAST** – Mass Spectrometer (SAMPEX)

**MLAT** – magnetic latitude

**MLT** – magnetic local time

**PET** – Proton/Electron Telescope (SAMPEX)

**RPA** – retarding potential analyzer

**RPI** – Radio Plasma Imager (SAMPEX)

**rpm** – rotations per minute

**SAMPEX** – Solar Anomalous and Magnetospheric Particle Explorer

**SETE** – subauroral electron temperature enhancement

**SM** – solar magnetic

**SSIES** – Special Sensor for Ions, Electrons, and Scintillation (DMSP)

**SSJ/4** – Special Sensor Precipitating Plasma Monitor (DMSP)

**SWEPAM** – Solar Wind Electron, Proton and Alpha Monitor (ACE)

**ULF** – ultra-low frequency

**UT** – Universal Time

**VLF** – very low frequency

# Chapter 8

## References

Anderson, P. C. (2007), personal communication.

Anderson, P. C., W. R. Johnston, J. Goldstein, and T. P. O’Brien (2007), Observations of the ionospheric projection of the plasmopause and comparisons with relativistic electron measurements, submitted to *JGR*.

Baker, D. N., R. W. Klebesadel, P. R. Higbie, and J. B. Blake (1986), Highly relativistic electrons in the earth’s outer magnetosphere, 1. Lifetimes and temporal history 1979-1984, *JGR*, **91**:4265-4276.

Baker, D. N., et al. (1993), An overview of the Solar, Anomalous, and Magnetospheric Particle Explorer (SAMPEX) Mission, *IEEE Trans. Geosci. & Remote Sens.*, **31**:531-541.

Baker, D. N., et al. (2004), An extreme distortion of the Van Allen belt arising from the “Hallowe’en” solar storm in 2003, *Nature*, **432**:878-881.

Beutier, T., and D. Boscher (1995), A three-dimensional analysis of the electron radiation belt by the Salammbô code, *JGR*, **100**(A8):14853-14861.

Brace, L. H., and R. F. Theis (1974), The behavior of the plasmopause at mid-latitudes:

ISIS-1 Langmuir probe measurements, *JGR*, **79**:1871-1884.

Brice, N. M. (1967), Bulk motion of the magnetosphere, *JGR*, **72**:5193-5211.

Burch, J. L., J. Goldstein, and B. R. Sandel (2004), Cause of plasmasphere corotation lag, *GRL*, **31**:L05802.

Carpenter, D. L. (1963), Whistler evidence of a “knee” in the magnetospheric ionization density profile, *JGR*, **68**:1675-1682.

Carpenter, D. L., and J. Lemaire (1997), Erosion and recovery of the plasmasphere in the plasmopause region, *Space Sci. Rev.*, **80**:153-179.

Carpenter, D. L., and C. G. Park (1973), On what ionosphere workers should know about the plasmopause-plasmasphere, *Rev. Geophys. & Space Phys.*, **11**:133-154.

Chappell, C. R., K. K. Harris, and G. W. Sharp (1971a), The dayside of the plasmasphere, *JGR*, **76**:7632-7647.

Chappell, C. R., K. K. Harris, and G. W. Sharp (1971b), OGO 5 measurements of the plasmasphere during observations of stable auroral red arcs, *JGR*, **76**:2357-2365.

Cook, W. R., et al. (1993), PET: A Proton/Electron Telescope for studies of magnetospheric, solar and galactic particles, *IEEE Trans. Geosci. & Remote Sens.*, **31**:565-571.

Davis, A., et al. (2007), *Ace Science Center* [<http://www.srl.caltech.edu/ACE/ASC/index.html>].

Dent, Z. C., I. R. Mann, J. Goldstein, F. W. Menk, and L. G. Ozeke (2006), Plasmaspheric depletion, refilling, and plasmopause dynamics: a coordinated ground-based and IMAGE satellite study, *JGR*, **111**:A03205.

Dessler, A. J., and B. J. O’Brien (1965), Penetrating particle radiation, in *Satellite Environment Handbook, 2nd ed.*, ed. by F. S. Johnson, 53-92, Stanford Univ. Press (Stanford, CA).

Foster, J. C., et al. (1978), Plasmopause signatures in the ionosphere and magnetosphere, *JGR*, **83**:1175-1182.

Fraser, B. J., and T. S. Nguyen (2001), Is the plasmopause a preferred source region of electromagnetic ion cyclotron waves in the magnetosphere?, *J. of Atm. & Solar-Terrestrial Phys.*, **63**:1225-1247.

Gallagher, D. L., M. L. Adrian, and M. W. Liemohn (2005), Origin and evolution of deep plasmaspheric notches, *JGR*, **110**:A09201.

Goldstein, J. (2004), Studying inner magnetospheric dynamics, ORBITALS workshop presentation, *Univ. of Alberta* [<http://www.phys.ualberta.ca/~orbitals/talks/goldstein01.pdf>].

Goldstein, J., J. L. Burch, and B. R. Sandel (2005a), Magnetospheric model of subauroral polarization stream, *JGR*, **110**(A9):A09222.

Goldstein, J., S. G. Kanekal, D. N. Baker, and B. R. Sandel (2005b), Dynamic relationship between the outer radiation belt and the plasmopause during March-May 2001, *GRL*, **32**:L15104.

Goldstein, J., and B. R. Sandel, (2005), The global pattern of evolution of plasmaspheric drainage plumes, in *Inner Magnetosphere Interactions: New Perspectives from Imaging*, ed. by J. Burch, M. Schulz, and H. Spence, 1-22, AGU (Washington, DC).

Goldstein, J., B. R. Sandel, M. R. Hairston, and P. H. Reiff (2003), Control of plasmaspheric dynamics by both convection and sub-auroral polarization stream, *GRL*, **30**(24):2243.

Grebowsky, J. M., J. H. Hoffman, and N. C. Maynard (1978), Ionospheric and magnetospheric “plasmapauses”, *Planet. Space Sci.*, **26**:651-660.

Gringauz, K. I. (1963), The structure of the ionized gas envelope of Earth from direct

measurements in the USSR of local charged particle concentrations, *Planet. Space Sci.*, **11**:281-96.

Hairston, M. (2006), Availability of the DMSP SSIES data, *Coupled Ion Neutral Dynamics Investigation* [<http://cindispace.utdallas.edu/DMSP/available.htm>].

Hardy, D. A., et al. (1984), *Precipitating electron and ion detectors (SSJ/4) for the Block 5D/flights 6-10 DMSP satellites: calibration and data presentation*, report AFGL-TR-84-0317, Air Force Geophysics Laboratory (Hanscom AFB, MA).

Hargreaves, J. K. (1992), *The solar-terrestrial environment*, Cambridge Univ. Press (Cambridge, MA).

Heelis, R. A., and W. B. Hanson (1998), Measurements of thermal ion drift velocity and temperature using planar sensors, in *Measurement Techniques in Space Plasmas: Particles*, ed. by R. F. Pfaff, J. E. Borovsky, and D. T. Young, 61-72, AGU (Washington, DC).

Horwitz, J. L., L. H. Brace, R. H. Comfort, and C. R. Chappell (1986), Dual-spacecraft measurements of plasmasphere-ionosphere coupling, *JGR*, **91**(A10):11203-11216.

Horwitz, J. L., et al. (1990a), Plasmasphere-ionosphere coupling 2. Ion composition measurements at plasmaspheric and ionospheric altitudes and comparison with modeling results, *JGR*, **95**(A6):7949-7959.

Horwitz, J. L., R. H. Comfort, and C. R. Chappell (1990b), A statistical characterization of plasmasphere density structure and boundary locations, *JGR*, **95**:7937-7947.

Jordanova, V. K., and Y. Miyoshi (2005), Relativistic model of ring current and radiation belt ions and electrons: Initial results, *GRL*, **32**:L14104.

Jordanova, V. K., et al. (2006), Kinetic simulations of ring current evolution during the Geospace Environment Modeling challenge events, *JGR*, **111**(A11):A11S10.

Karpachev, A. T., and L. N. Sidorova (2003), Distinction and classification of the



troughs and subtroughs in  $\text{He}^+$  density from ISS-b satellite data at 1000-1200 km altitudes, *J. of Atm. & Solar-Terrestrial Phys.*, **65**:997-1006.

Kelley, M. C., and R. A. Heelis (1989), *The Earth's Ionosphere: Plasma Physics and Electrodynamics*, Academic Press (San Diego, CA).

Kohnlein, W., and W. J. Raitt (1977), Position of the mid-latitude trough in the topside ionosphere as deduced from ESRO 4 observations, *Planet. Space Sci.*, **25**:600-602.

Lemaire, J. F., and K. I. Gringauz (1998), *The Earth's plasmasphere*, Cambridge Univ. Press (Cambridge, MA).

Li, X., D. N. Baker, S. G. Kanekal, M. Looper, and M. Temerin (2001), Long term measurements of radiation belts by SAMPEX and their variations, *GRL*, **28**(20):3827-3830.

Li, X., D. N. Baker, and M. Temerin (1997), Multisatellite observations of the outer zone electron variation during the November 3-4, 1993, magnetic storm, *JGR*, **102**:14123-14140.

Li, L., and R. L. Xu (2005), Model of the evolution of the plasmasphere during a geomagnetic storm, *Adv. Space Res.*, **36**:1895-1899.

Lyons, L. R., and R. M. Thorne (1973), Equilibrium structure of radiation belt electrons, *JGR*, **78**(13):2142-2149.

Margolies, D. L., and T. von Rosenvinge (1998), Advanced Composition Explorer (ACE): Lessons learned and final report, NASA/Goddard (Greenbelt, MD).

McComas, D. J., et al. (1998), Solar Wind Electron Proton Alpha Monitor (SWEPAM) for the Advanced Composition Explorer, *Space Sci. Rev.*, **86**:563-612.

McKay, M. F., D. S. McKay, and M. B. Duke (1992), *Space Resources: Energy, Power, and Transport*, Report SP-509, Vol. 2, NASA (Houston, TX).

Mewaldt, R. (1993), The Proton Electron Telescope (PET) on SAMPEX: Users document, *SAMPEX Data Center* [<http://www.srl.caltech.edu/sampex/DataCenter/docs/PET-UsersDocument.pdf>].

Miyoshi, Y. S., et al. (2006), Observations and modeling of energetic electron dynamics during the October 2001 storm, *JGR*, **111**(A11):A11S02.

Moldwin, M. B., M. F. Thomsen, S. J. Barne, D. J. McComas, and K. R. Moore (1994), An examination of the structure and dynamics of the outer plasmasphere using multiple geosynchronous satellites, *JGR*, **99**:11475-11481.

Nakamura, R., et al. (2000), SAMPEX observations of precipitation bursts in the outer radiation belt, *JGR*, **105**(A7):15875-15885.

Nishida, A. (1966), Formation of plasmopause, or magnetospheric plasma knee, by the combined action of magnetospheric convection and plasma escape from the tail, *JGR*, **71**:5669-5679.

O'Brien, T. P., et al. (2003), Energization of relativistic electrons in the presence of ULF power and MeV microbursts: Evidence for dual ULF and VLF acceleration, *JGR*, **108**(A8):1329-1342.

O'Brien, T. P., and M. B. Moldwin (2003), Empirical plasmopause models from magnetic indices, *GRL*, **30**(4):1152.

Rasmussen, C. E., S. M. Guiter, and S. G. Thomas (1993), A two-dimensional model of the plasmasphere: refilling time constants, *Planet. Space Sci.*, **41**:35-43.

Rycroft, M. J., and S. J. Burnell (1970), Statistical analysis of movements of the ionospheric trough and plasmopause, *JGR*, **75**:5600-5604.

SAMPEX Data Center (2007), SAMPEX pointing modes and history, *SAMPEX Data Center* [[http://www.srl.caltech.edu/sampex/DataCenter/docs/SAMPEX\\_pointing-](http://www.srl.caltech.edu/sampex/DataCenter/docs/SAMPEX_pointing-)

history2.pdf].

Sandel, B. R., et al. (2000), The Extreme Ultraviolet Imager investigation for the IMAGE mission, *Space Sci. Rev.*, **91**:197-242.

Sandel, B., T. Forrester, and T. Bavaro (2006), Image EUV Online Catalog, *IMAGE Extreme Ultraviolet Imager* [<http://euv.lpl.arizona.edu/euv/>].

Sandel, B. R., J. Goldstein, D. L. Gallagher, and M. Spasojevic (2003), Extreme ultraviolet imager observations of the structure and dynamics of the plasmasphere, *Space Sci. Rev.*, **109**:25-46.

Schulz, M., and L. J. Lanzerotti (1974), *Particle Diffusion in the Radiation Belts*, Springer-Verlag (New York, NY).

Spjeldvik, W. N., and P. L. Rothwell (1985), Chapter 5, The radiation belts, in *Handbook of Geophysics and Space Physics*, ed. by A. S. Jursa, 5.1-5.55, Air Force Systems Command (Washington, DC).

Smith, C. W., et al. (1998), The ACE Magnetic Fields Experiment, *Space Sci. Rev.*, **86**:613-632.

Stern, D. P. (1975), The motion of a proton in the equatorial magnetosphere, *JGR*, **80**:595-599.

Stone, E. C., et al. (1998), The Advanced Composition Explorer, *Space Sci. Rev.*, **86**:1-22.

Summers, D., and C. Ma (2000), A model for generating relativistic electrons in the Earth's inner magnetosphere based on gyroresonant wave-particle interactions, *JGR*, **105**(A2):2625-2639.

Summers, D., B. Ni, and N. P. Meredith (2007a), Timescales for radiation belt electron acceleration and loss due to resonant wave-particle interactions: 1. Theory, *JGR*,

**112**:A04206.

Summers, D., B. Ni, and N. P. Meredith (2007b), Timescales for radiation belt electron acceleration and loss due to resonant wave-particle interactions: 2. Evaluation for VLF chorus, ELF hiss, and electromagnetic ion cyclotron waves, *JGR*, **112**:A04207.

Summers, D., R. M. Thorne, and F. Xiao (1998), Relativistic theory of wave-particle resonant diffusion with application to electron acceleration in the magnetosphere, *JGR*, **103**(A9):20487-20500.

Tascione, T. F. (1988), *Introduction to the Space Environment*, Krieger Pub. Co.

Taylor, H. A., Jr., and W. J. Walsh (1972), The light ion trough, the main trough, and the plasmapause, *JGR*, **77**:6716-6723.

Toffoletto, F., S. Sazykin, R. Spiro, and R. Wolf (2003), Inner magnetospheric modeling with the Rice Convection Model, *Space Sci. Rev.*, **107**:175-196.

Tsyganenko, N. A., and M. I. Sitnov (2005), Modeling the dynamics of the inner magnetosphere during strong geomagnetic storms, *JGR*, **110**(A3):A03210.

Van Allen, J. A. (1959), The geomagnetically trapped corpuscular radiation, *JGR*, **64**:1683-89.

Volland, H. (1973), A semiempirical model of large-scale magnetospheric electric *JGR*, **78**:171-180.

Walt, M. (1996), Source and loss processes for radiation belt particles, in *Radiation Belts: Models and Standards*, ed. by J. F. Lemaire, D. Heynderickx, and D. N. Baker, 1-13, AGU (Washington, DC).

Weimer, D. R., et al. (2003), Predicting interplanetary magnetic field (IMF) propagation delay times using the minimum variance technique, *JGR*, **108**(A1):1026.

Weygand, J. (2007), Weimer et al. [2003] propagated solar wind, *Institute of Geophysics*

*and Planetary Physics* [<http://www.igpp.ucla.edu/solarwind.htm>].

WDC for Geomagnetism, Kyoto (2007), Geomagnetic Data Service, *WDC for Geomagnetism, Kyoto* [<http://swdcwww.kugi.kyoto-u.ac.jp/wdc/Sec3.html>].

Yizengaw, E., et al. (2005), The correlation between mid-latitude trough and the plasmopause, *GRL*, **32**:L10102.

Yizengaw, E., and M. B. Moldwin (2005), The altitude extension of the mid-latitude trough and its correlation with plasmopause position, *GRL*, **32**:L09105.